Ore Geology Reviews 153 (2023) 105269

Contents lists available at ScienceDirect

Ore Geology Reviews

journal homepage: www.elsevier.com/locate/oregeorev

Multivariate statistical analysis of trace elements in apatite: Discrimination of apatite with different origins

Hou Ming Rui Tan [a,b], Xiao-Wen Huang [a,*], Yu-Miao Meng [a], Huan Xie [a,b], Liang Qi [a]

[a] State Key Laboratory of Ore Deposit Geochemistry, Institute of Geochemistry, Chinese Academy of Sciences, Guiyang 550081, China
[b] University of Chinese Academy of Sciences, Beijing 100049, China

ARTICLE INFO

Keywords:
Apatite
Origins
Rock types
Deposit types
Discrimination
PLS-DA

ABSTRACT

Partial least squares-discriminant analysis (PLS-DA) was used to construct the link between trace element contents of magmatic or hydrothermal apatite and deposit and rock types. Apatite with different origins is discriminated by characteristic chemical composition. In average, ore magmatic apatite has higher light REE and Th, and lower Sr than barren rock apatite, independent of deposit types. Hydrothermal apatite has lower La, Ce, Pr, and Nd contents than magmatic apatite, probably because fluids prefer migrating light rare earth element out of apatite. Hydrothermal apatite from iron oxide copper gold (IOCG) and iron oxide apatite (IOA) deposits is discriminated by high Mn and Sr relative to magmatic apatite, probably because these elements are fluid mobile. Barren magmatic apatite from granitoid-related deposits is well separated from ore magmatic apatite by higher Sr, Eu, Gd, Tb, Dy, and lower Mn contents, which are likely related to the relatively low degree of differentiation and high aluminum saturation index of parental magma.

Magmatic apatite from IOA deposits is discriminated by relatively high Nd, Sm, Gd, Tb, Dy, and low Mn and U contents, which are possibly related to the crystallization of Mn-compatible magnetite microlites and peraluminous magmas. Magmatic apatite from granitoid-related W deposits is relatively rich in Y, Sm, Gd, Tb, Dy, Ho, Er, Tm, Yb, and Lu. The relative enrichment of Sr in magmatic apatite from granitoid-related Cu-Pb-Zn and Pb-Zn deposits is likely due to less fractionation of Sr-compatible plagioclase. Melt of sediment component accounts for high Mn and Th in magmatic apatite from granitoid-related Mo deposits. Magmatic apatite from porphyry deposits is discriminated by relatively high V, Sr, and Eu contents. Magmatic apatite from porphyry Mo deposits has relatively high Pr, Nd, and Sm and low Sr contents compared to other types of porphyry deposits due to the more evolved magma. Hydrothermal apatite from IOA deposits is discriminated by high V and Sr, whereas those from IOCG deposits have high Sm, Eu, Gd, Tb, and U contents, because the lower temperature of IOCG cause precipitation of REE in Cl-rich fluid. Relatively low Gd and Tb in hydrothermal apatite from skarn deposits are possibly due to the crystallization of amphibole.

Apatite in carbonatite has high contents of trace elements possibly because high contents of Ca and P in melts cause high apatite-melt partition coefficients of trace elements. Apatite from sedimentary and metamorphic rocks is discriminated by relative enrichment of Sr and Eu. Compared to igneous rocks, apatite from sedimentary rocks has low REE contents, reflecting low REE budget in surface waters. Breakdown of some minerals to release and remobilize REE and U during metamorphism can interpret high heavy REE and U contents in apatite from high-grade metamorphic rocks relative to those from low- and medium-grade metamorphic rocks. The ability to discriminate apatite from different types of deposits and rocks indicates the application potential of apatite chemistry in mineral exploration. A flowchart was proposed to identify apatite with unknown origins.

1. Introduction

Apatite [$Ca_{10}(PO_4)_6(F, Cl, OH)$] is a ubiquitous mineral in igneous, metamorphic, and sedimentary rocks (Bouzari et al., 2016; Webster and Piccoli, 2015), and it can also form by biomineralization (Elliott, 2002; Hughes and Rakovan, 2002; Piccoli and Candela, 2002). Apatite can be stable in weathering and transport in the surface environment (Belousova et al., 2002; Mao et al., 2016), which makes apatite become an

---

* Corresponding author.
E-mail address: huangxiaowen@vip.gyig.ac.cn (X.-W. Huang).

https://doi.org/10.1016/j.oregeorev.2022.105269
Received 28 July 2022; Received in revised form 17 December 2022; Accepted 18 December 2022

ideal indicator mineral. Early crystallized magmatic apatite is weakly affected by later alteration and metamorphism, and thus preserves the information of the parental magma (Ayers and Watson, 1993; Watson and Green, 1981). The Mn content, Ce, and Eu anomalies in apatite are used to indicate the relative oxygen fugacity of the magmatic rock related to mineralization (Cao et al., 2012; Pan et al., 2016; Sha and Chappell, 1999; Xing et al., 2021). In addition, the contents of major and trace elements in apatite can discriminate different types of rocks and deposits and evaluate the mineralization potential of the host rocks (Belousova et al., 2002; Cao et al., 2012; Chappell and White, 1992; Jiang et al., 2018; Mao et al., 2016; O'Sullivan et al., 2020; Pan et al., 2016; Piccoli and Candela, 2002).

As an important indicator mineral, numerous studies have been carried out for apatite origin discrimination. Contents of Na, Ca, Sr, Cr, and Ni, Fe^{3+}/Fe^{2+} ratio, REE patterns, and element ratios (e.g., La/Y, Sm/Nd) are used to discriminate apatite from different types of granite (Chappell and White, 1992; Sha and Chappell, 1999). Eu/Eu* and Ce/Ce* of apatite is used to constrain the oxygen fugacity of the crystallization environment (Cao et al., 2012). Based on the contents of Sr, Y, Mn, total REE, REE pattern and the Eu anomaly of apatite, Belousova et al. (2002) used correlation and regression trees to classify different types of rocks. Machine learning methods such as principal component analysis, support vector machine, and decision tree algorithm are used to discriminate deposit types, and rock types and determine whether the rocks are mineralization-related (Mao et al., 2016; O'Sullivan et al., 2020). These results provide a good basis for apatite origin discrimination.

In this study, LA-ICP-MS trace element data of apatite from the published literature were systematically collected. The large dataset was investigated by partial least squares-discriminant analysis (PLS-DA) to link apatite chemistry with their origins (i.e., magmatic versus hydrothermal, barren versus mineralization, different types of deposits and rocks). The factors controlling variations in the chemical composition of apatite were discussed. Some PLS-DA diagrams with good discrimination for deposit or rock types can be used to constrain the origin of apatite without known background information, which will be important for quick screening in mineral exploration.

2. Data preparation

2.1. Date source

A total of 4298 data were collected from different types of deposits and rocks (Appendix 1). These deposits and rocks hosting apatite are from different countries and areas: Australia, Brazil, Canada, Chile, China, Finland, France, Germany, Greece, Greenland, Iceland, Iran, Italy, Kazakhstan, New Zealand, Norway, Peru, Russia, Scotland, Sweden, Ukraine, USA, and Mid-Atlantic Ridge (Fig. 1, Appendix 1). We divide apatite into ore and barren magmatic apatite, hydrothermal apatite according to the mineralization potential of hosted rock, and the origin of hydrothermal or magmatic (Appendix 2). The number of magmatic apatite is 1801 and 101 for silicate rocks and carbonatite, respectively. Apatite data of sedimentary and metamorphic rocks are 108 and 360, respectively. The number of hydrothermal apatite from porphyry, IOA, skarn, IOCG, and orogenic Au deposits is 117, 498, 302, 32, and 808, respectively. This classification is used to constrain the factors controlling magmatic and hydrothermal processes, and the factors related to mineralization. Ore magmatic apatite is defined as apatite in the magmatic rocks genetically related to mineralization, whereas barren magmatic apatite refers to apatite from magmatic rocks not related to mineralization. Barren rock apatite means apatite from magmatic, sedimentary, and metamorphic rocks absent of mineralization. Hydrothermal apatite includes primary hydrothermal apatite and secondary hydrothermal altered apatite. Deposit type classification is used to discuss the main controlling factors for different types of mineralization. The deposit types include iron oxide-apatite (IOA), iron oxide-copper–gold (IOCG), porphyry, orogenic Au, skarn, and granitoid-related deposits (Fig. 2). Granitoid-related deposits have W, Mo, Cu-Pb-Zn, and Pb-Zn subtypes, whereas porphyry deposits include Cu, Cu-Au, Cu-Mo, Mo-Cu, Mo, and Au-polymetallic subtypes. Skarn deposits include Au-Co, W, and Pb-Zn subtypes. Rock type classification is used to constrain different rock-forming processes. Rock types are divided into igneous, carbonatite, sedimentary, and metamorphic rocks. Igneous rocks are further divided into acid-alkaline, acid calcium-alkaline, intermediate alkaline, intermediate calcium-alkaline, basic alkaline, basic calcium-alkaline, and ultrabasic rocks according to silicon content and alkalinity. Metamorphic rocks are divided into two subtypes: low- and

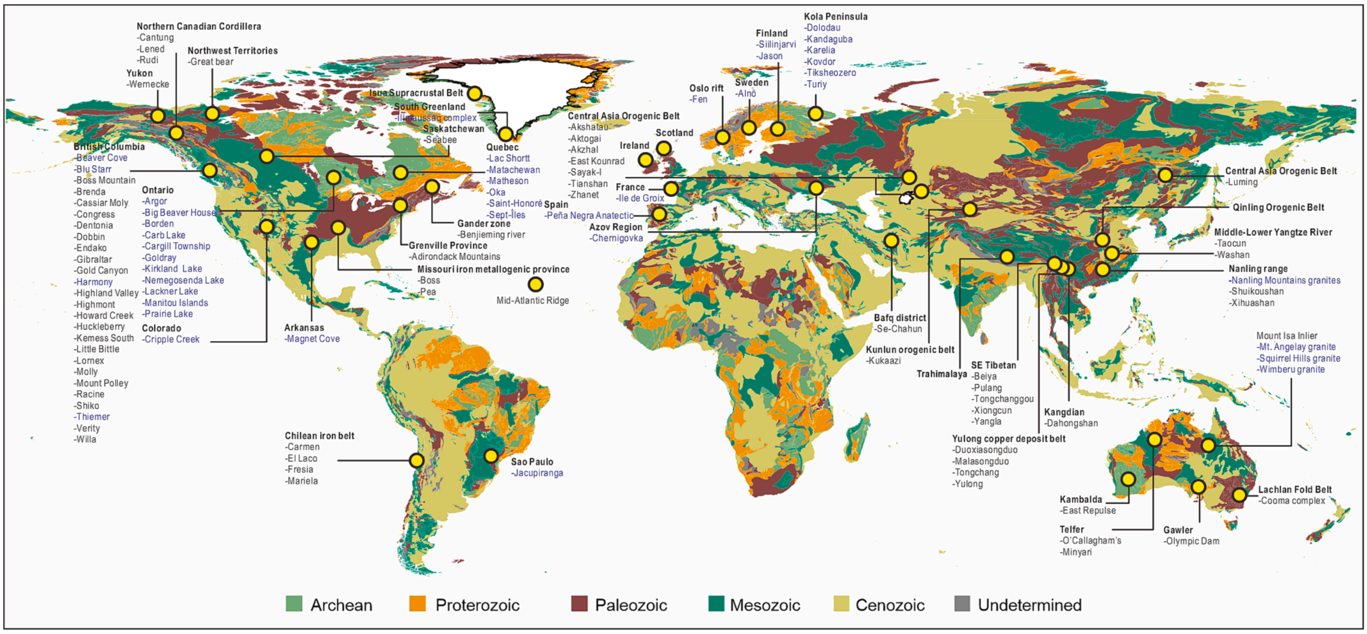

Fig. 1. Distribution of selected deposits and rocks. Blue color highlights regions of unmineralized rocks. The physical map of world is from M. Colpron (Geological Survey of Canada). (For interpretation of the references to color in this figure legend, the reader is referred to the web version of this article.)

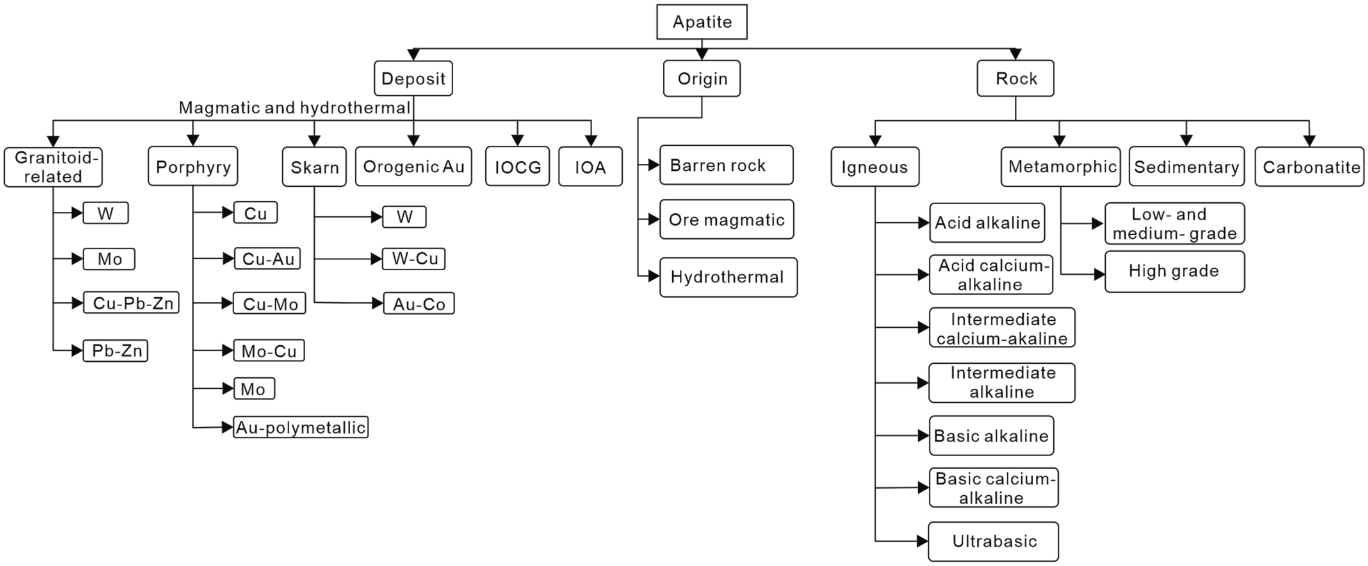

Fig. 2. Classification of apatite by different origins.

medium-grade metamorphic rocks and high-grade metamorphic, based on the degree of metamorphism.

2.2. Data preprocessing and partial least squares-discriminant analysis

Apatite LA-ICP-MS data include censored data that are below detection limits or null (Helsel, 2005). Elements V, Mn Sr, Y, La, Ce, Pr, Nd, Sm, Eu, Gd, Tb, Dy, Ho, Er, Tm, Yb, Lu, Th, and U contain less than 40 % censored values were imputed using the R-software package robCompositions (Hron et al., 2010; Makvandi et al., 2016). The centered-log ratio (clr) method was used for data conversion to eliminate the correlation between elements inherited from concentration calculation (Aitchison, 1982; Egozcue et al., 2003; Makvandi et al., 2016; Whitten, 1995). PLS-DA is carried out using the procedure similar to those described in Huang et al. (2019). PLS-DA is used to distinguish magmatic versus hydrothermal apatite, barren and ore apatite, and apatite from the different deposit and rock types.

Different from the unsupervised classification method, supervised PLS-DA uses predefined data (De Iorio et al., 2007) to extract orthogonal components (latent variables), and construct the link between the X (N × K) and Y (N × M) matrices by maximizing the covariance (Brereton and Lloyd, 2014; Eriksson et al., 2013; Wold et al., 2001):

$$X = TP^T + E$$

$$Y = TQ^T + F$$

$$T = XW^*$$

where T (N × r) is the matrix containing r orthogonal PLS components (scores) and represents the common latent variable space of both X and Y. P (N × r) and Q (M × r) represent the loading matrices for X and Y. The weight matrix (W*) is the linear regression coefficients of the X variables that best predicts Y. E and F mean the respective model residuals for X and Y.

Loadings biplots (e,g., qw^*_1, qw^*_2) display the correlations among elements and illustrate the relationship between elements and defined groups (Eriksson et al., 2013). Sample distribution in the score plots (e.g., t_1 versus t_2) is controlled by the correlation among elements in the loading plot (Eriksson et al., 2013). The score contribution plot highlights the relative enrichment (positive score contribution) or depletion (negative score contribution) of elements in a specific group. The variable importance on the projection (VIP) plot summarizes the importance of elements in classifying the predefined group. Elements having VIP values >1 are interpreted as be the most important in the classification.

Multiple steps of PLS-DA are carried out based on the origins of apatite (Fig. 2). First, PLS-DA is used to discriminate ore magmatic, barren rock, and hydrothermal apatite independent of deposit types. The discrimination between apatite from these three origins was further evaluated based on specific deposit types. Second, PLS-DA is used to distinguish different deposit types and subtypes. Third, PLS-DA is used to distinguish rock types and their subtypes.

3. Results

3.1. Trace element composition of apatite

Fig. 3 shows the minimum, maximum, median, and average contents of V, Mn, As, Rb, Sr, Y, Zr, Pb, Th, U, Ba, and W which have less than 60 % censored data. Ore magmatic apatite has relatively high median Mn (708 ppm) and Th (19 ppm) contents, whereas barren rock apatite has relatively high median V (16.6 ppm), Zr (4 ppm), Pb (12.5 ppm), and Ba (11 ppm) contents (Fig. 3a). Hydrothermal apatite has higher median As (97 ppm) and W (1.4 ppm) than ore magmatic apatite (Fig. 3a). Fig. 3b shows contents of elements in magmatic and hydrothermal apatite from different deposits. Apatite from IOA deposits have relatively high median V (18.4 ppm), As (191.4 ppm), and W (3.5 ppm) contents (Fig. 3b), whereas those from IOCG deposits have relatively high median W (2.5 ppm) and low median Th (1.2 ppm) contents (Fig. 3b). Apatite from skarn deposits is characterized by relatively high median Mn (1290 ppm) and low median V (0.3 ppm), As (4.5 ppm), and W (0.2 ppm) contents (Fig. 3b). Apatite from porphyry deposits has higher median V (21.5 ppm), Sr (544.6 ppm), and Zr (1.2 ppm) contents than others. Apatite from orogenic Au deposits is discriminated by high median Y (1190 ppm) and U (20.4 ppm) contents (Fig. 3b). Apatite from granitoid-related deposits has relatively high median Pb (9.2 ppm) and Th (51.9 ppm) contents (Fig. 3b).

Apatite from igneous rocks is characterized by relatively high median V (5.4 ppm), Y (724 ppm), Pb (4.8 ppm), Th (23.3 ppm), and U (14.1 ppm) contents (Fig. 3c). Apatite from carbonatite is characterized by relatively high median V (5.3 ppm), Sr (4897 ppm), Zr (1.5 ppm), and Th (20.4 ppm) and low W (less than 0.01 ppm) contents (Fig. 3c). Apatite from sedimentary rocks has relatively high median As (89.3 ppm), Ba (46 ppm) and Th (0.2 ppm) contents, whereas those from metamorphic rocks have relatively high median Mn (1225 ppm) and low

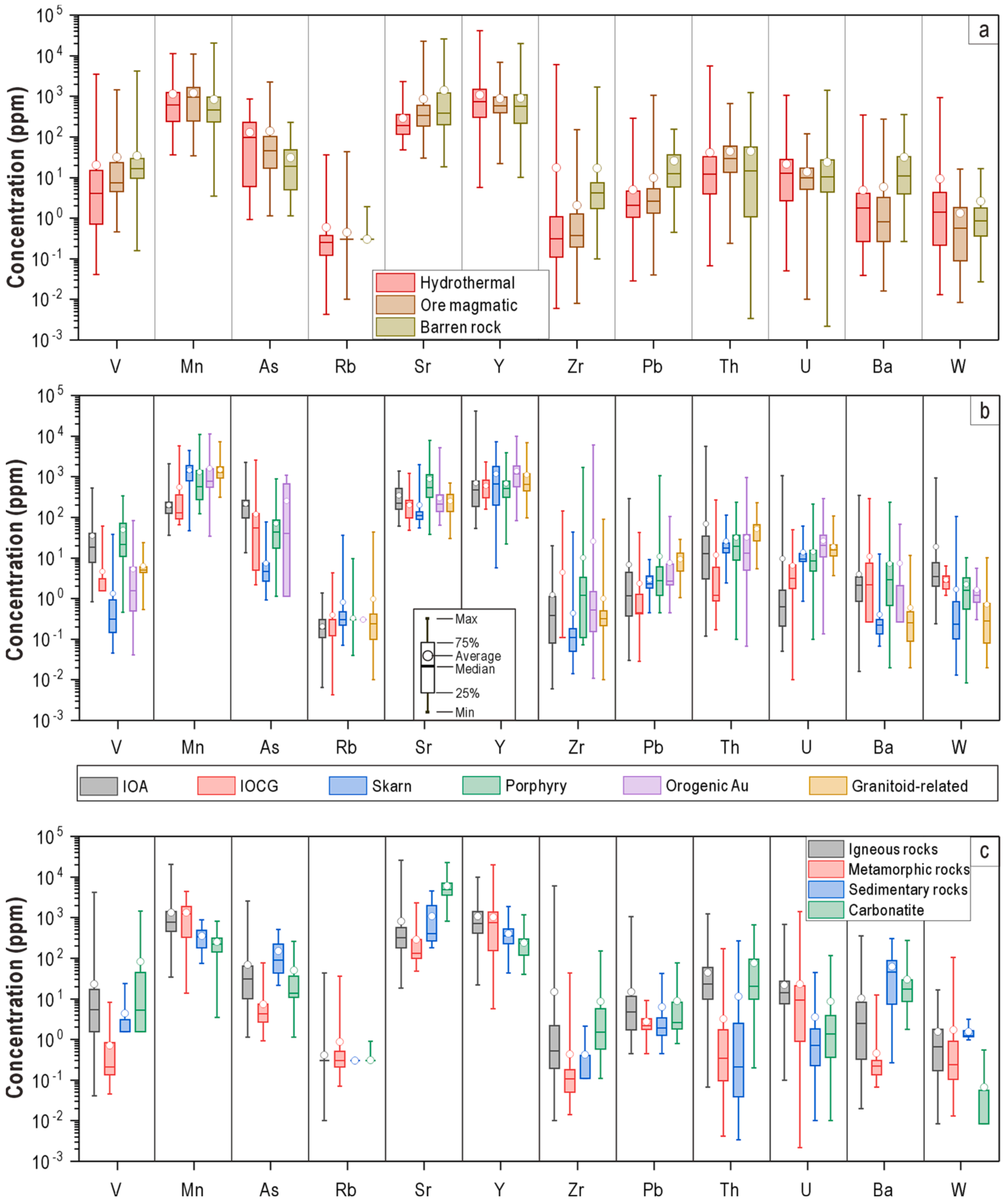

Fig. 3. Box and whisker plots for LA-ICP-MS trace element data of apatite from barren rock, ore magmatic, and hydrothermal origins (a), different types of deposits (b), and different types of rocks (c) Boxes outline the 25th to 75th percentiles and whiskers extend to the minimum and maximum values. Short line within the box represents the median value, whereas circle filled by white on the whisker represents the average value. Trace element contents below the limit of detection were removed from the box and whisker plots.

V (0.2 ppm), As (4.3 ppm), Sr (131.8 ppm), Zr (0.1 ppm), and Ba (0.2 ppm) contents (Fig. 3c).

Chondrite-normalized REE spider diagrams for individual analyses and median contents of apatite are shown in Figs. 4-6. Barren rock, ore magmatic apatite, and hydrothermal apatite, show LREE-rich patterns with negative Eu anomaly (Fig. 4a-c). Ore magmatic and barren rock apatite have higher LREE but lower HREE than hydrothermal apatite (Fig. 4d). Hydrothermal apatite shows stronger Eu depletion than ore magmatic and barren rock apatite (Fig. 4d). Ore magmatic apatite has higher LREE contents than barren rock apatite but shows similar Eu negative anomaly (Fig. 4a, b, d).

Apatite from IOA, IOCG, and orogenic Au deposits show LREE-rich patterns with negative Eu anomaly (Fig. 5a, c). Apatite from porphyry and granitoid-related deposits also show LREE-rich pattern with negative Eu anomaly but has higher REE contents than apatite from IOA, IOCG, and orogenic Au deposits. The Tb, Ho, Er, and Tm anomalies in apatite from granitoid-related Pb-Zn, porphyry Cu-Mo, and Mo deposits are probably due to lacking data (Fig. 5d, e). The REE patterns of apatite from different types of porphyry deposits are similar. REE contents of apatite from granitoid-related Mo deposits are higher than those from other granitoid-related deposits (Fig. 5d). The chondrite-normalized LREE of apatite from different porphyry deposits vary within one order of magnitude (Fig. 5e). Apatite from porphyry Mo-W deposits has the highest REE contents and strongest Eu negative anomaly, whereas those from porphyry Au-polymetallic deposits have the weakest negative Eu anomaly (Fig. 5e). Apatite from skarn W and Au-Co deposits has LREE-rich patterns, whereas that from skarn W deposits shows up-concave patterns (Fig. 5f). The REE content of apatite from skarn W-

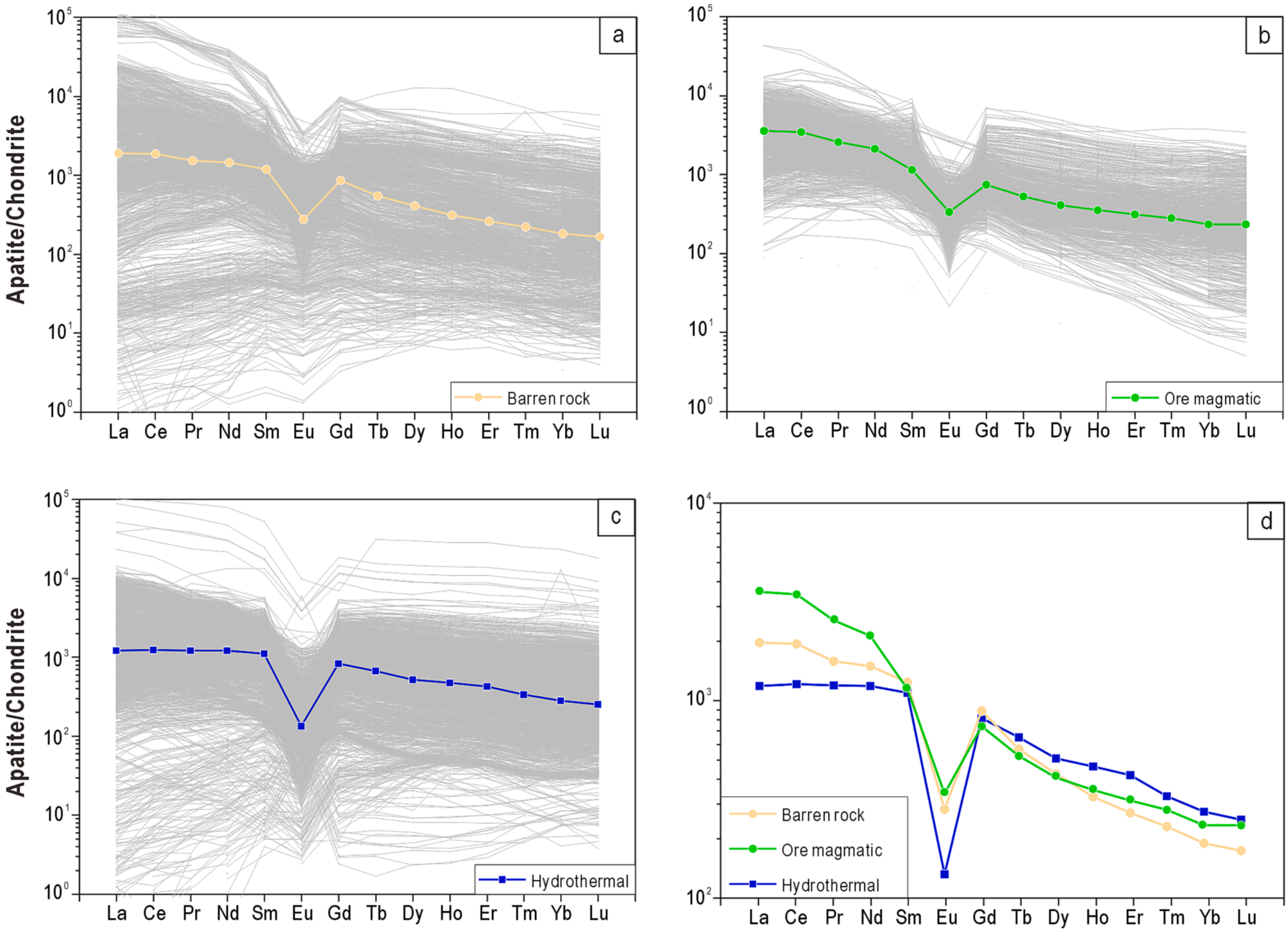

Fig. 4. Chondrite-normalized REE plots for median (color lines) and individual (gray lines) values of barren rock (a), ore magmatic (b), and hydrothermal apatite (c). (d) Comparison between median REE values of barren rock, ore magmatic, and hydrothermal apatite.

Cu deposits is lower than apatite from other skarn deposits (Fig. 5f). Moreover, apatite from skarn W-Cu deposits has stronger negative Eu anomalies than that from skarn W and Au-Co deposits (Fig. 5f).

REE patterns of most apatite from igneous rocks, carbonatite, and sedimentary rocks are LREE-rich and Eu depleted (Fig. 6a, b, d), whereas those from metamorphic rocks are up-concave (Fig. 6b). Apatite from basic alkaline igneous rocks has higher REE content and stronger negative Eu anomaly than those from other igneous rocks (Fig. 6a). Apatite in acid alkaline, acid calcium-alkaline, intermediate alkaline, intermediate calcium-alkaline, basic alkaline, basic calcium-alkaline, and ultrabasic rocks has similar REE patterns (Fig. 6a). Apatite from ultrabasic igneous rocks has the lowest REE content and weakest negative Eu anomaly (Fig. 6a). Apatite from low- and medium- grade metamorphic rocks have similar REE patterns with apatite from high grade metamorphic rocks, but the former has lower total REE contents and weaker negative Eu anomaly (Fig. 6b). The REE pattern of carbonatite is similar to ultrabasic rocks, which is characterized by weak negative Eu negative anomaly and HREE depletion (Fig. 6c). Apatite from igneous rocks have higher REE contents than metamorphic and sedimentary rocks (Fig. 6a, c). Apatite in igneous and metamorphic rocks has negative Eu anomalies, whereas those from sedimentary rocks and carbonatite have no significant Eu anomaly (Fig. 6).

3.2. PLS-DA results of apatite composition

3.2.1. Magmatic and hydrothermal apatite

As shown in Fig. 7a, b, barren rock, ore magmatic, and hydrothermal apatite cannot be discriminated from each other in the plot of the first and second PLS-DA components. In terms of average composition, barren rock apatite is characterized by relatively high Sr, Eu, and U contents (Fig. 7a). Ore magmatic apatite show relative enrichment of Th, Eu, La, Ce, Pr, and Nd (Fig. 7a), whereas hydrothermal apatite is relatively rich in Gd, Tb, Dy, Ho, Er, Tm, Yb, Lu, and Y (Fig. 7a).

3.2.2. Apatite from IOCG and IOA deposits grouped by ore magmatic and hydrothermal

Ore magmatic, barren rock, and hydrothermal apatite independent of deposit types are not well separated by PLS-DA, so further PLS-DA analysis is carried out for the specific deposit types. Despite overlapping of apatite compositions of ore magmatic and hydrothermal apatite from IOCG and IOA deposits in t_1–t_2 (Fig. 8a, b). Ore magmatic apatite mainly plots on the positive side of t_1 due to positive correlation with La, Ce, Pr, Nd, and U (Fig. 8a, b).

3.2.3. Apatite from granitoid-related deposits grouped by barren and ore magmatic

Ore and barren magmatic apatite can be distinguished by PLS-DA on t_1-t_2 (Fig. 9a, b). Barren apatite is discriminated by the relative enrichment of U and Eu and the relative depletion of Mn, La, Ce, Pr, and Nd, in contrast to the chemical feature of ore magmatic apatite (Fig. 9c, d).

3.2.4. Apatite from porphyry deposits grouped by barren magmatic, ore magmatic, and hydrothermal apatite

There is significant compositional overlapping among the three types of apatite (Fig. 10a, b). Compared to the average of the dataset, barren magmatic apatite is characterized by relative enrichment of Sr and Eu

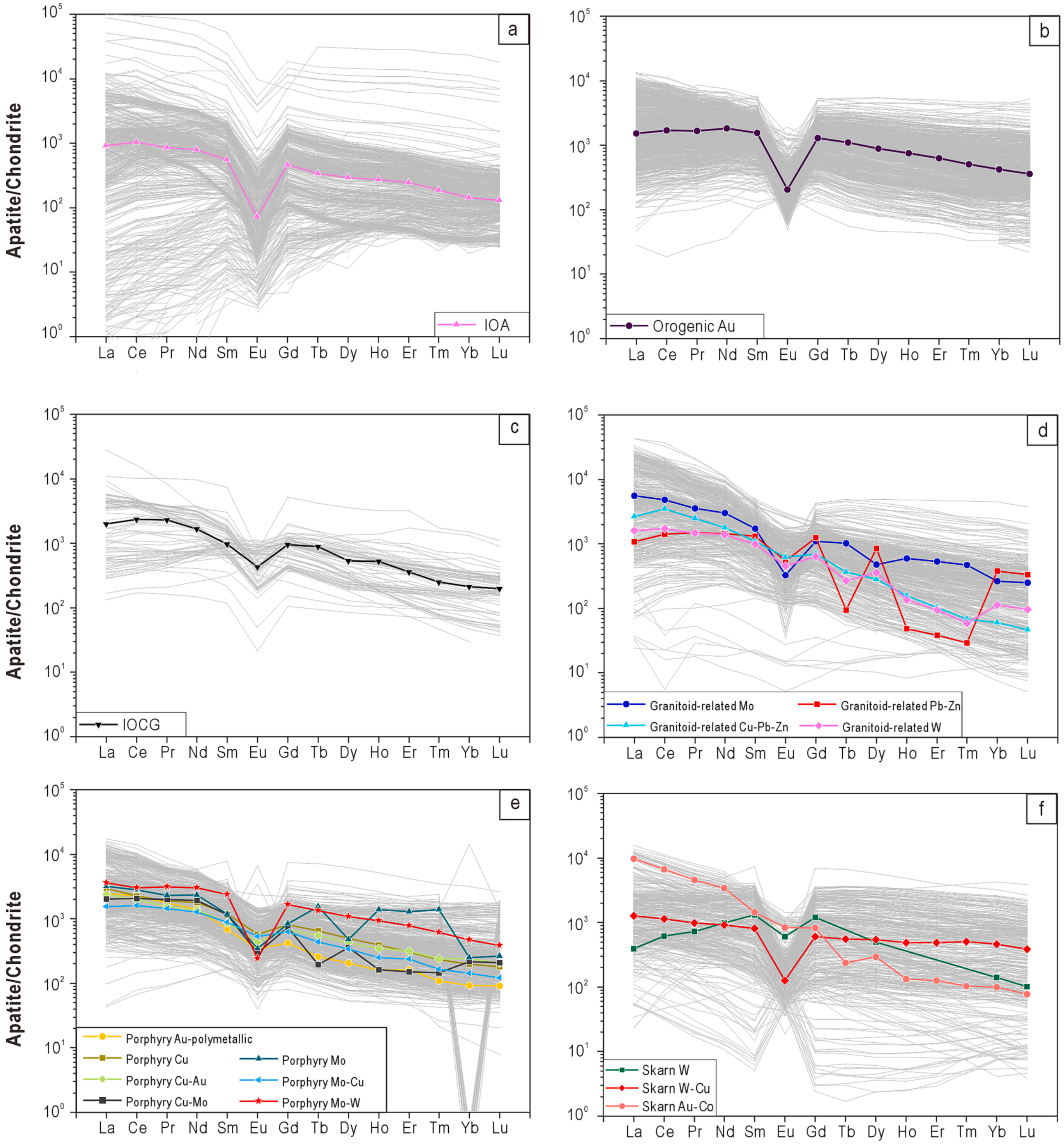

Fig. 5. Chondrite-normalized REE plots for median values of apatite from IOA (a), orogenic Au (b), IOCG (c), granitoid-related (d), porphyry (e), and skarn (f) deposits. The gray lines represent individual analyses.

(Fig. 10a). Ore magmatic apatite shows relatively high V content (Fig. 10a), whereas hydrothermal apatite has relatively high Eu and low V contents (Fig. 10a).

3.2.5. Magmatic apatite grouped by deposit types without subtypes

The deposit types include porphyry (Cu, Cu-Au, Cu-Mo, Mo-Cu, Mo, Au-polymetallic), granitoid-related (W, Mo, Cu-Pb-Zn, and Pb-Zn), orogenic gold, IOCG, IOA, and skarn (W, W-Cu) deposits. Magmatic apatite from porphyry deposits is separated from other types in the t_1-t_2 plot due to the positive correlation with V, Sr, and Eu (Fig. 11a, b). Magmatic apatite from granitoid-related deposits mainly plots in the positive t_1 region due to the positive correlation with LREE in spite of partial overlapping with magmatic apatite from porphyry and skarn deposits (Fig. 11c, d). Magmatic apatite from IOA deposits is separated from other deposit types in the t_1-t_3 plot because of negative correlation with Mn and U (Fig. 11c, d). The score contribution plots show that magmatic apatite from granitoid-related deposits is relatively rich in La, Ce, Pr, and Nd, and depleted in V, Sr, and Eu (Fig. 11e), in contrast to

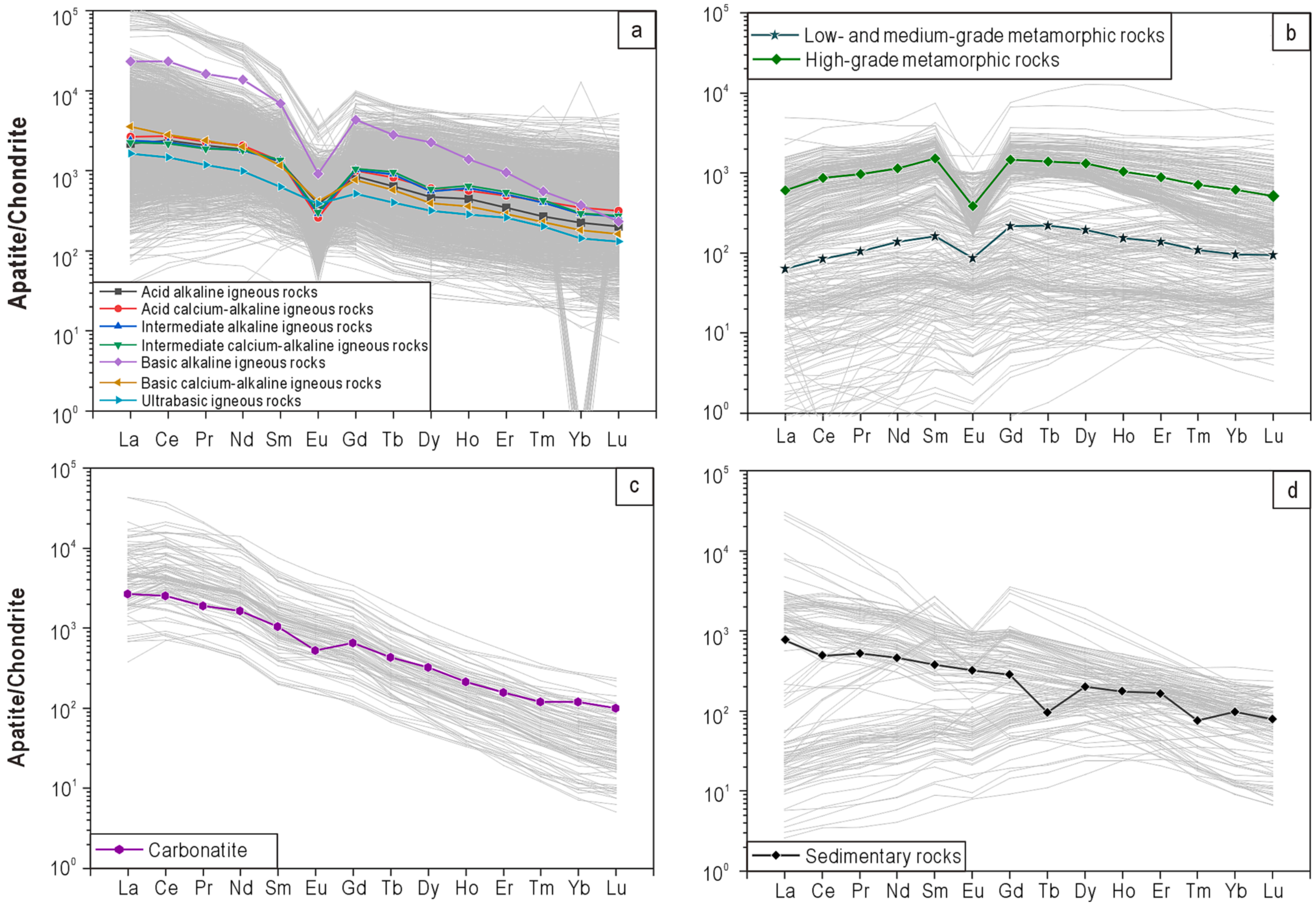

Fig. 6. Chondrite-normalized REE plots for median values of apatite from igneous rocks (a), metamorphic rocks (b), carbonatite (c), and sedimentary rocks (d). The gray lines represent individual analyses.

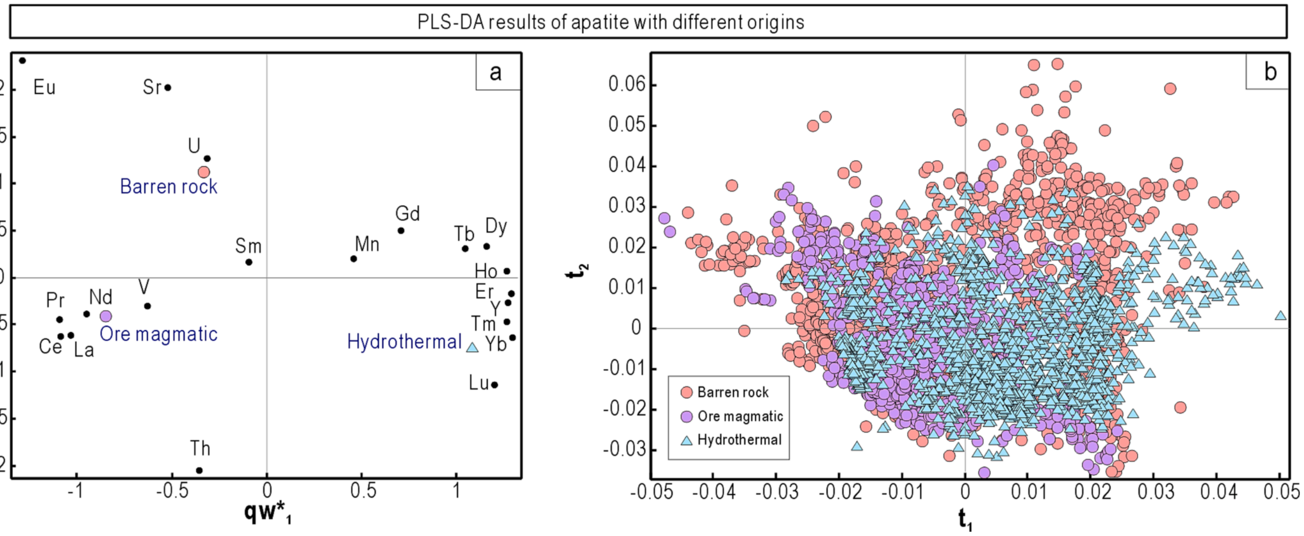

Fig. 7. PLS-DA results of chemical composition of barren rock, ore magmatic, and hydrothermal apatite. (a) Plot of qw^*_1 vs qw^*_2 (first and second loadings) showing correlation among elements and origins of apatite. (b) Plot of t_1 vs t_2 (first and second scores) showing the distribution of individual analyses of apatite in the latent variable space defined by qw^*_1–qw^*_2 in (a).

magmatic apatite from porphyry deposits (Fig. 11g). Magmatic apatite from IOA deposits shows relative enrichment of Sm, Eu, Gd, Tb, Dy, Ho, Er, Tm, Yb, and Lu. VIP plot shows that V, Mn, Sr, Th, U, La, Ce, Pr, Nd, Sm, Eu, and Lu are important elements in discriminating the defined deposit types (Fig. 11*h*).

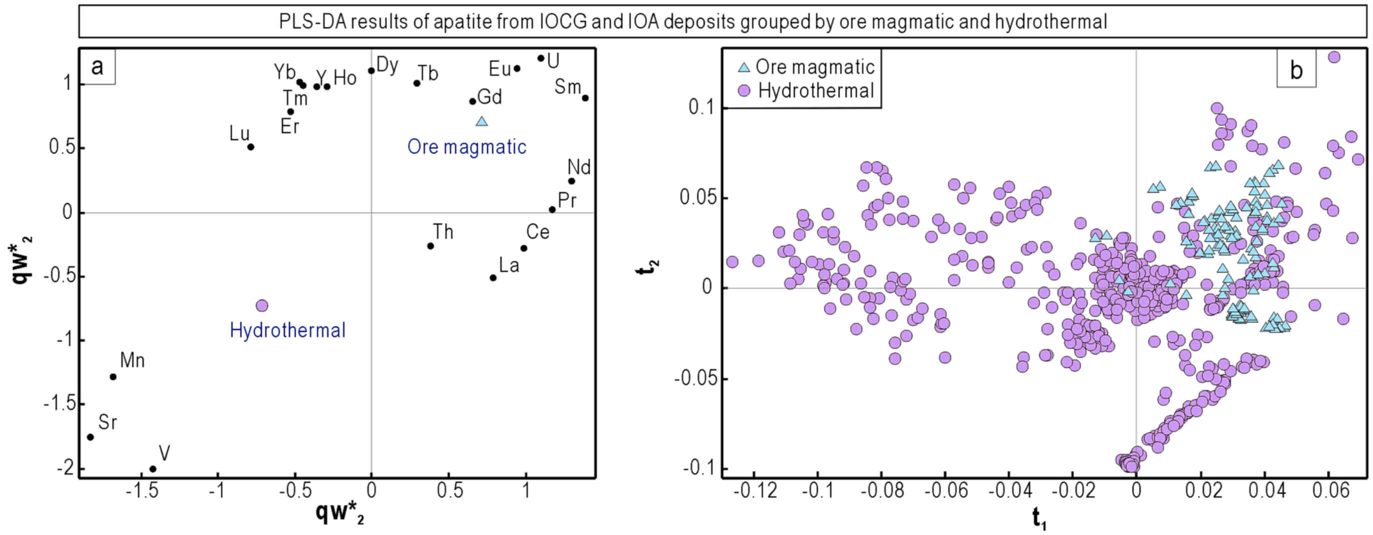

Fig. 8. PLS-DA results of chemical composition of ore magmatic and hydrothermal apatite of IOCG and IOA deposits. (a) Plot of qw*$_1$ vs qw*$_2$ (first and second loadings) showing correlation among elements and origins of apatite. (b) Plot of t_1 vs t_2 (first and second scores) showing the distribution of individual analyses in the latent variable space defined by qw*$_1$–qw*$_2$ in (a). For projection of unknown samples, please see the Appendix 3.

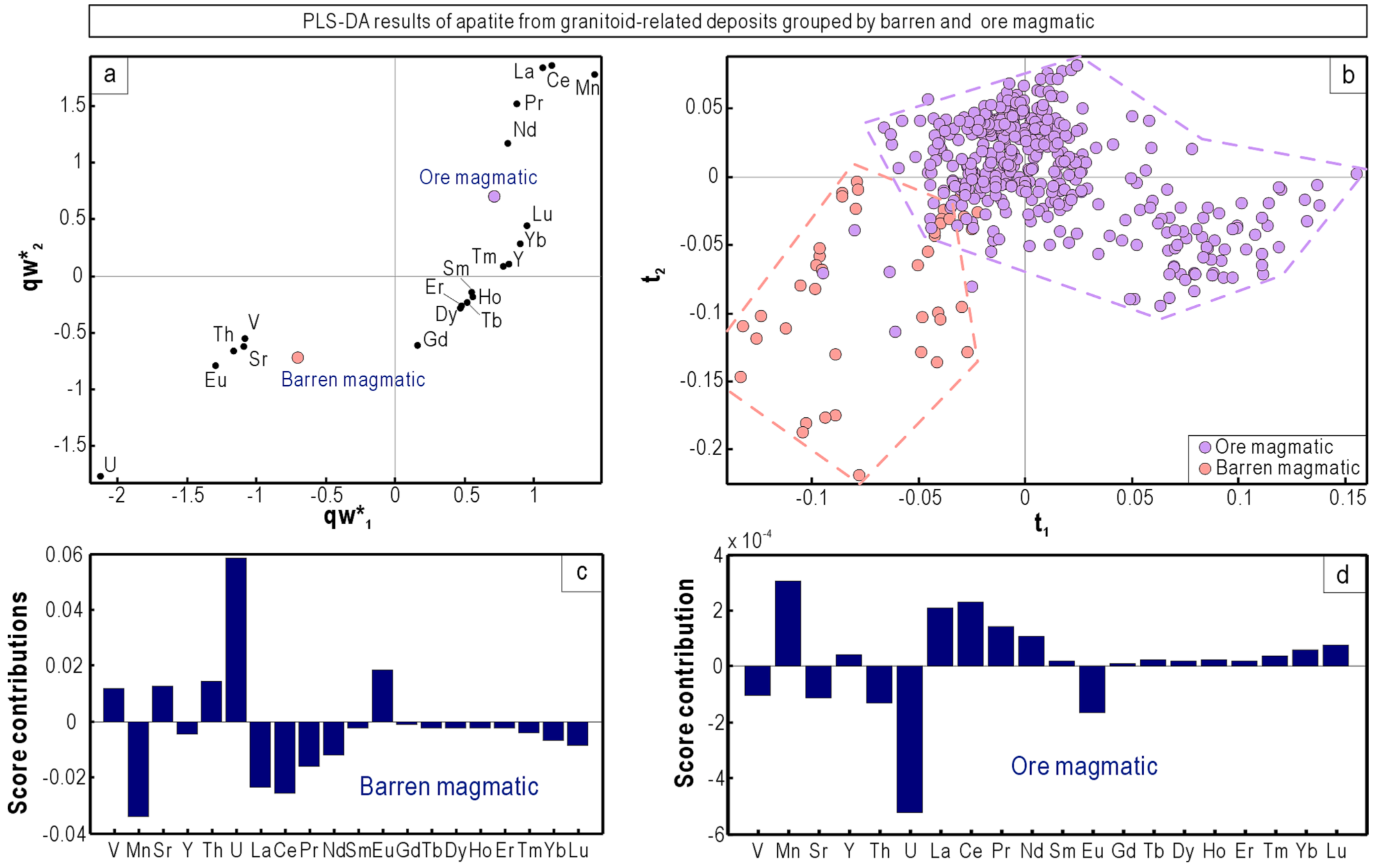

Fig. 9. PLS-DA results of chemical composition of ore and barren magmatic apatite from granitoid-related deposits. (a) Plot of qw*$_1$ vs qw*$_2$ (first and second loadings) showing correlation among elements and origins of apatite. (b) Plot of t_1 vs t_2 (first and second scores) showing the distribution of individual analyses in the latent variable space defined by qw*$_1$–qw*$_2$ in (a). (c-d) Score contribution plots of elements for different origins of granitoid-related deposits. For projection of unknown samples, please see the Appendix 3.

3.2.6. Hydrothermal apatite grouped by deposit types without subtypes

Hydrothermal apatite from IOA deposits is separated from other deposit types in the t_1-t_2 plot because of positive correlation with V and Sr (Fig. 12a, b, f). Those from IOCG, orogenic Au, porphyry Cu-Au, and skarn (W-Cu, Au-Co) deposits cannot be discriminated in this plot. However, hydrothermal apatite from skarn deposits can be well discriminated in t_1-t_3 by the positive contribution of Mn and negative contribution of V in spite of partial overlapping with orogenic Au and

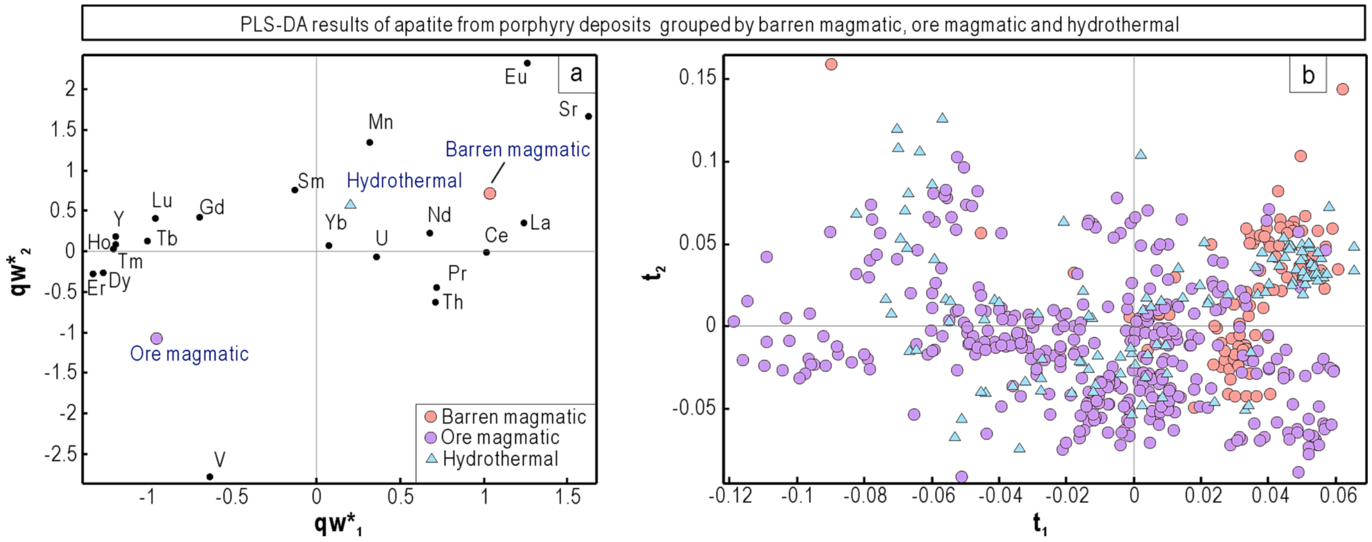

Fig. 10. PLS-DA results of chemical composition of barren magmatic, ore magmatic, and hydrothermal apatite of porphyry deposits. (a) Plot of qw*$_1$ vs qw*$_2$ (first and second loadings) showing correlation among elements and origins of apatite. (b) Plot of t_1 vs t_2 (first and second scores) showing the distribution of individual analyses in the latent variable space defined by qw*$_1$–qw*$_2$ in (a).

porphyry deposits (Fig. 12 c, d, g). Hydrothermal apatite from IOCG deposits plots in the positive t_1, negative t_3 region because of positive contributions of Sm, Eu, Gd, Tb, and Dy (Fig. 12c, e). The VIP diagram shows that V, Mn, Sr, Sm, Gd, and U are important discriminant elements in the classification (Fig. 12h).

3.2.7. *Magmatic apatite grouped by deposit types with subtypes*

To evaluate the classification effect of deposit subtypes, we divide granitoid-related deposits into four subtypes, skarn deposits into two subtypes, and porphyry deposits into six subtypes. Combined with undivided IOCG, IOA, and orogenic Au deposits, a total of 15 deposit types/subtypes are used for PLS-DA. Magmatic apatite from granitoid-related W deposits is separated from other subtypes of granitoid-related deposits by t_1 because they are negatively correlated to V, Sr, and Eu (Fig. 13a, b, h). Magmatic apatite from skarn W-Cu deposits is also separated from that from skarn W deposits by t_1 because of relatively high Y, Sm, Gd, Tb, Dy, Ho, Er, Tm, Lu but low La, Ce, Pr, and Eu contents (Fig. 13a, b, m). Magmatic apatite from IOCG and IOA deposits mainly plots in negative t_3 region due to positive correlation with Sm, Gd, Tb, Dy, Ho, Er, and negative correlation with Mn, and U (Fig. 13c, d, i, j). Magmatic apatite from porphyry Cu-Mo deposits plots in negative t_4 region, as a result of positive correlation with Mn and negative correlation with Th (Fig. 13e, f, k). All elements except Yb are important in the classification (Fig. 13n).

3.2.8. *Hydrothermal apatite grouped by deposit types with subtypes*

The PLS-DA results of hydrothermal apatite grouped by deposit types with subtypes are similar to Fig. 12 where subtypes are not considered. Hydrothermal apatite from IOA deposits is located in negative t_1 because of high V and Sr, but low U contents (Fig. 14a, d, g). Hydrothermal apatite from skarn W-Cu deposits can be well discriminated in t_1-t_3 due to the positive correlation with Mn and negative correlation with V and Sr (Fig. 14c, d, i). Hydrothermal apatite from IOCG deposits plot in the positive t_1 and negative t_4 region due to positively correlated Sm, Eu, Gd, Tb, and U (Fig. 14e, f, h). VIP plot displays that V, Mn, Sr, Sm, Eu, Gd, and U are important elements for discriminating most deposit types (Fig. 14j).

3.2.9. *Magmatic apatite grouped by granitoid-related deposit subtypes*

Some deposit subtypes are not well discriminated by PLS-DA when considering all the deposit types. Hence, we try to discriminate subtypes within a specific deposit type. The data of magmatic apatite define three different fields in t_1-t_2: (1) Apatite from granitoid-related W deposits plotting in the right side of t_1 are discriminated by positive contributions of Y, Sm, Gd, Tb, Dy, Ho, Er, Tm, Yb and Lu (Fig. 15a, b, d, h); (2) Apatite from granitoid-related Mo deposits mainly plot in the positive side of t_2 because of positive contributions of Mn and Th, but negative contributions of Sm and Gd (Fig. 15a, b, e); (3) Apatite from granitoid-related Cu-Pb-Zn and Pb-Zn deposits in the negative t_2 region due to positive correlation with Sr and U (Fig. 15a, b, f, g). Apatite from granitoid-related Pb-Zn deposits plotting in the negative t_3 because of positive correlation with Sr, Th, and U (Fig. 15c, d, f, g). VIP plot shows that except V, all analyzed elements show variable importance for the studied deposit types (Fig. 15i).

3.2.10. *Magmatic apatite grouped by porphyry deposit subtypes*

Apatite from porphyry Cu-Mo and porphyry Mo deposits plots in the positive side of t_1 due to relatively high Mn, Sm, and Gd and low Sr, U (Fig. 16a, b). Apatite from porphyry Cu-Au deposits clusters in the negative t_2 because of positive correlation with V and U, and negative correlation with Mn, Pr, Nd, and Sm (Fig. 16a, b, e). Apatite from porphyry Mo deposits plotting in the positive t_3 is discriminated from that from porphyry Cu-Mo deposits because the former is negatively correlated with Sr and Eu (Fig. 16c, d, f, g). The VIP diagram shows that Mn, Sr, Sm, Eu, and Yb are important elements in the discriminant analysis (Fig. 16h).

3.2.11. *Apatite grouped by rock types without subtypes*

We classify the rocks hosting apatite into four groups: igneous, carbonatite, metamorphic, and sedimentary rocks. PLS-DA results show that apatite in igneous rocks and carbonatite is distinguished in t_1-t_2, whereas those from metamorphic and sedimentary rocks are overlapped (Fig. 17a, b). The score contribution plot shows that positive La, Ce, Pr, Nd, and Th, and negative Sr and Eu contributions discriminate apatite from igneous rocks (Fig. 17c). Apatite from carbonatite is relatively rich in Sr and Eu but depleted in Tm, Lu, and U (Fig. 17d). Apatite from metamorphic rocks shows negative contributions of La, Ce, Pr, Nd, Sm, and Th (Fig. 17e), whereas those from sedimentary rocks show positive Sr and Eu but negative La, Ce, Pr, and Nd contributions (Fig. 17f). VIP plot demonstrate that Sr, La, Ce, Pr, Nd, Eu, and Th are important discriminant elements for different types of rocks (Fig. 17g).

3.2.12. *Apatite grouped by rock types with subtypes*

In order to distinguish the compositional differences of apatite

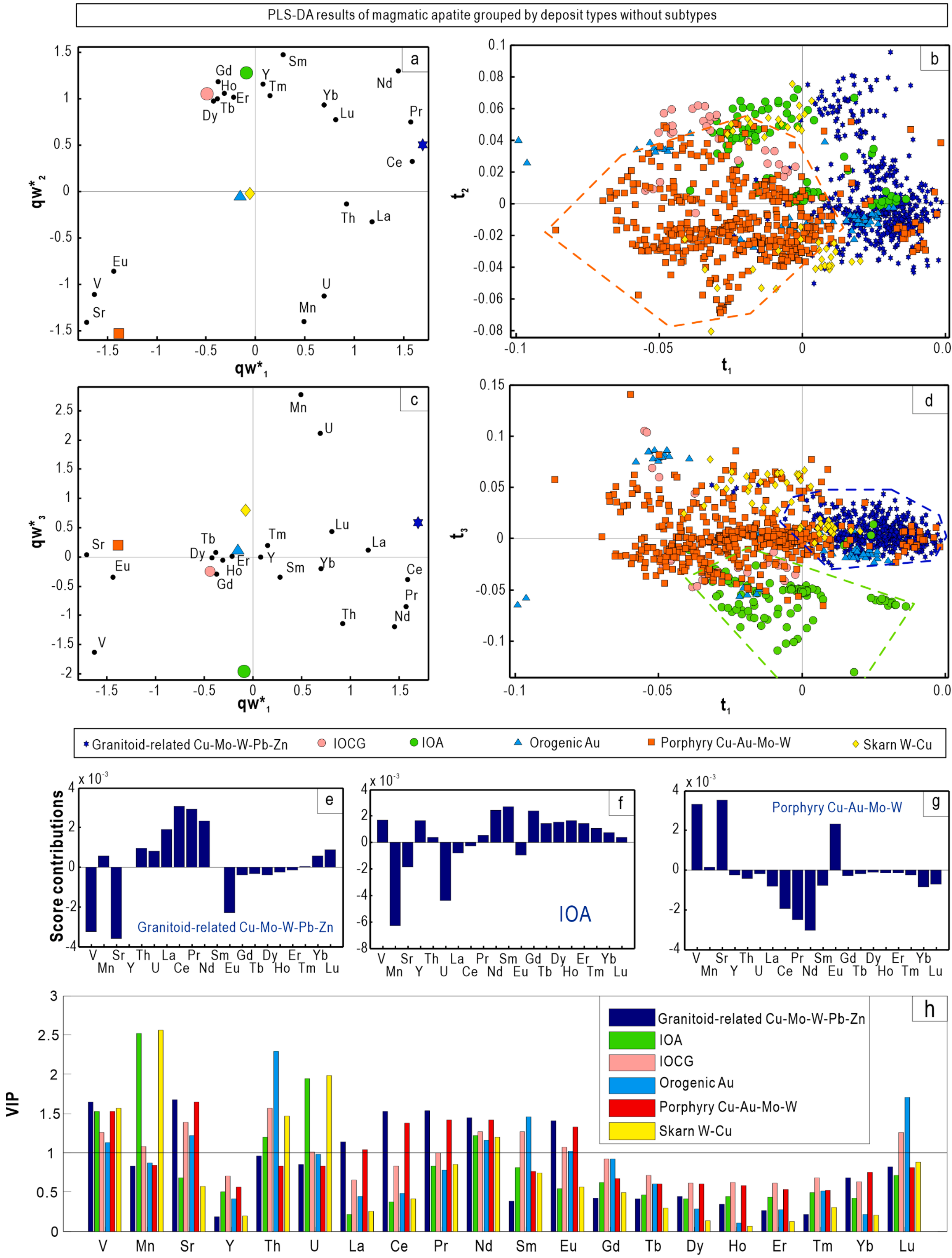

Fig. 11. PLS-DA results of magmatic apatite grouped by deposit types without subtypes. (a) Plot of qw*$_1$ vs qw*$_2$ (first and second loadings) showing correlation among elements and deposit types. (b) Plot of t_1 vs t_2 (first and second scores) showing the distribution of individual analyses from different types of deposits in the latent variable space defined by qw*$_1$–qw*$_2$ in (a). (c) Plot of qw*$_1$ vs qw*$_3$ (first and third loadings) showing correlation among elements and deposit types. (d) Plot of t_1 vs t_3 (first and third scores) showing the distribution of individual analyses from different types of deposits in the latent variable space defined by qw*$_1$–qw*$_3$ in (c). (e-g) Score contribution plots of elements for the selected deposit types. (h) The VIP plot showing the importance of elements in the classification. Gray line marks VIP value of one (the same as below). For projection of unknown samples, please see the Appendix 3.

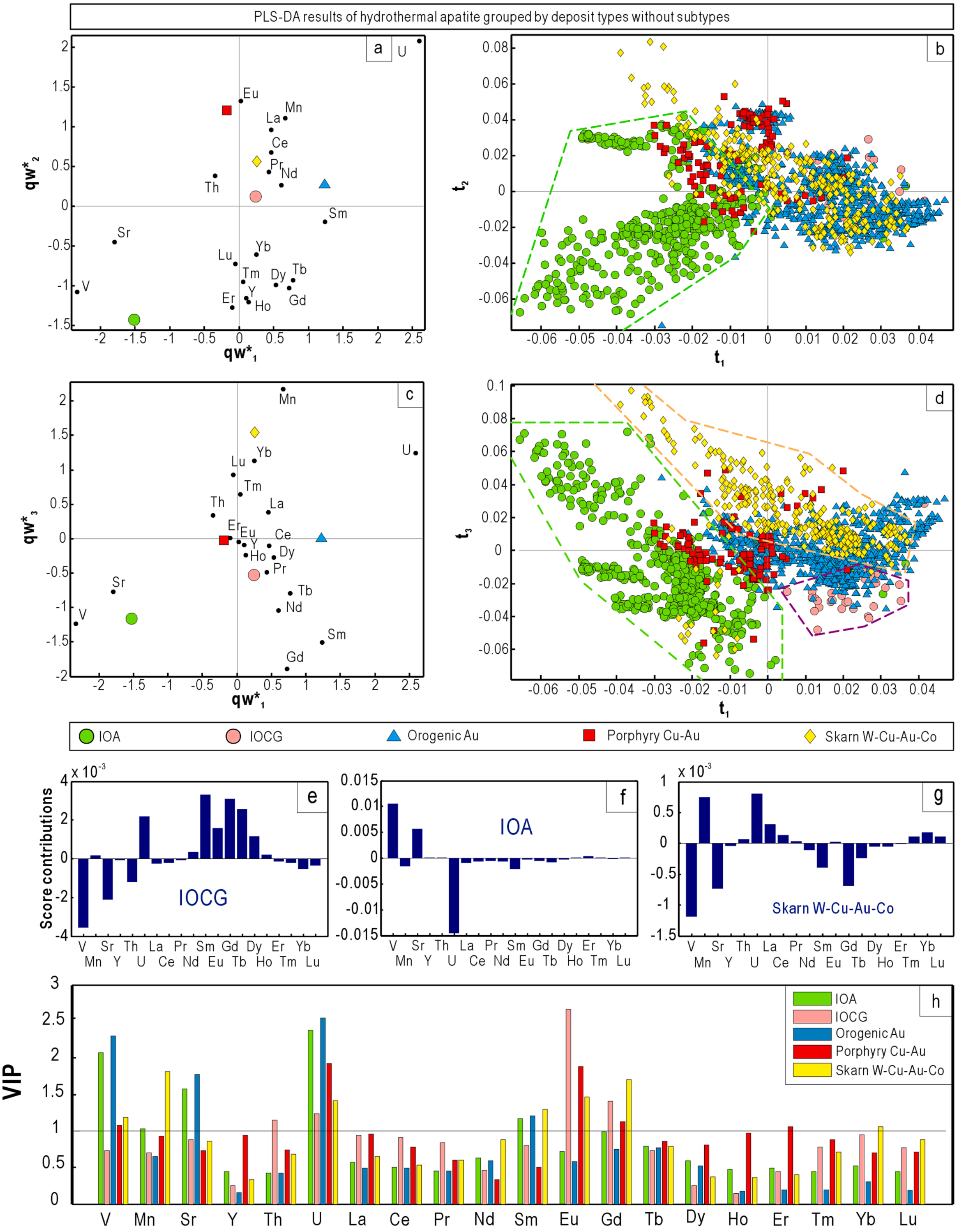

Fig. 12. PLS-DA results of hydrothermal apatite chemical composition grouped by deposit types without subtypes. (a) Plot of qw^*_1 vs qw^*_2 (first and second loadings) showing correlations among element variables and deposit types. (b) Plot of t_1 vs t_2 (first and second scores) showing the distribution of individual analyses from different deposits in the latent variable space defined by qw^*_1–qw^*_2 in (a). (c) Plot of qw^*_1 vs qw^*_3 (first and third loadings) showing correlations among element variables and deposit types. d Plot of t_1 vs t_3 (first and third scores) showing the distribution of individual analyses from different deposits in the latent variable space defined by qw^*_1–qw^*_3 in (c). (e-g) Score contribution plots of elements for well discriminated deposits. (h) The VIP showing the importance of compositional variables in classification. For projection of unknown samples, please see the Appendix 3.

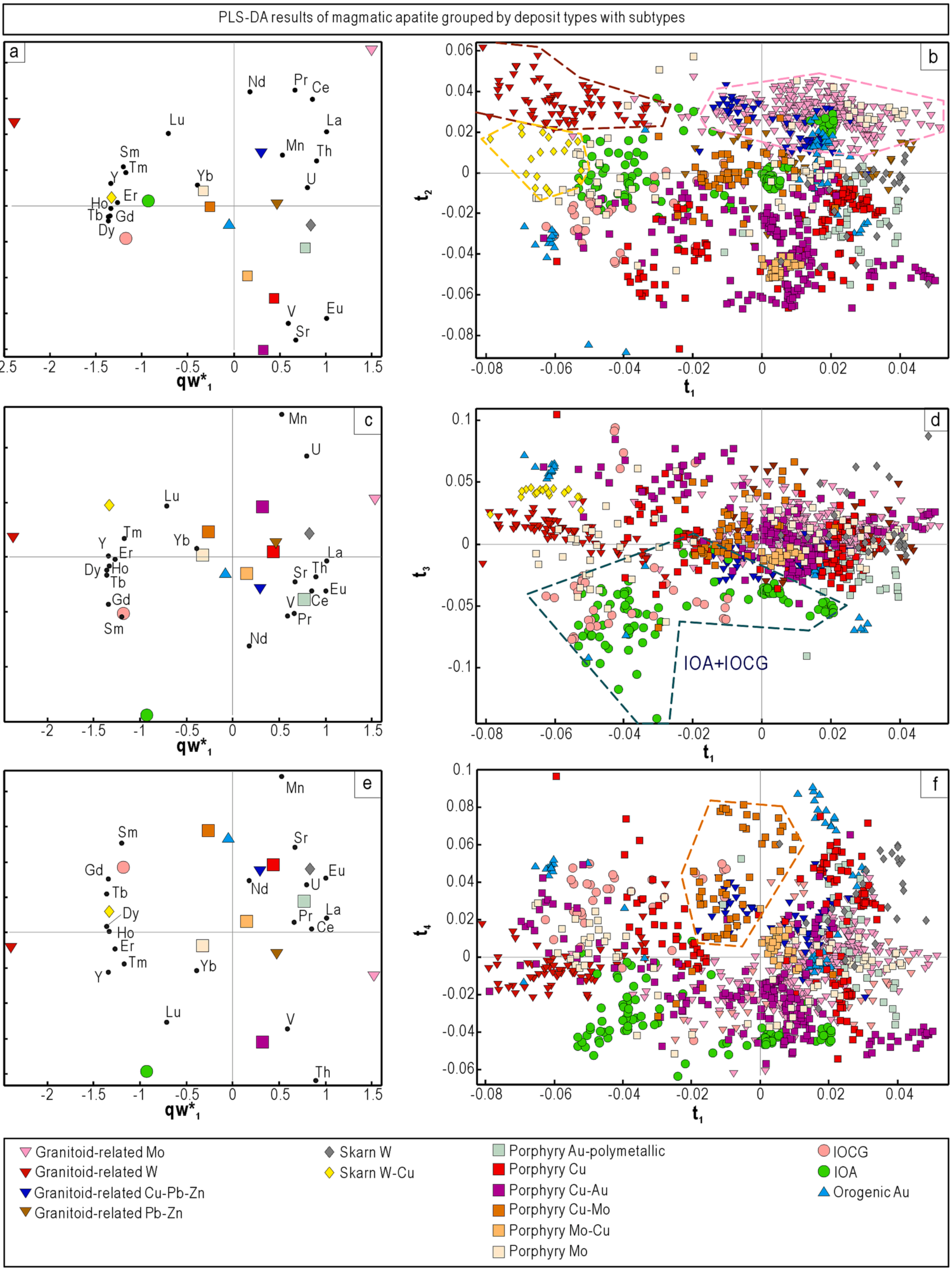

Fig. 13. PLS-DA results of magmatic apatite grouped by deposit types with subtypes. Plots of first and second loadings (a), first and third loadings (c), first and fourth loadings (e) showing correlations among elements and deposit types. Plots of first and second scores(b), first and third scores (d), first and fourth scores (f) showing the distribution of individual analyses from different types of deposits in the latent variable space defined in (a), (c) and (e), respectively. (g-m) Score contribution plots of elements for the selected deposit types. (n) The VIP plot showing the importance of elements in classification. For projection of unknown samples, please see the Appendix 3.

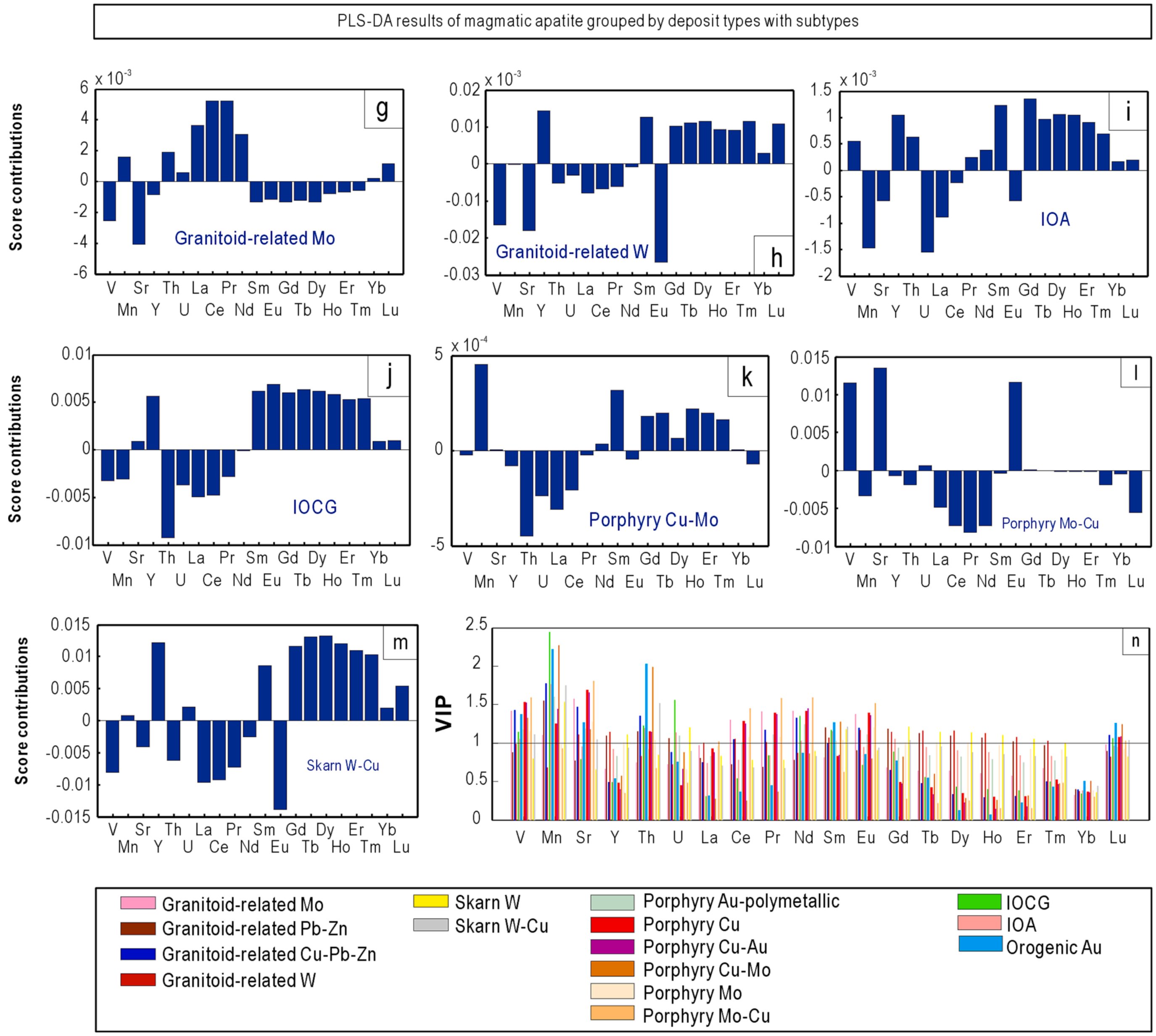

Fig. 13. (*continued*).

between different subtypes of igneous and metamorphic rocks, PLS-DA analysis is carried out for a total of 11 groups of rocks. Similar to the results in Fig. 17, apatite from carbonatite is separated from those from other rock types (Fig. 18a, b). Apatite from sedimentary rocks overlaps with apatite from low- and medium-grade metamorphic rocks (Fig. 18a, b). Subtypes of igneous and metamorphic rocks cannot be well discriminated by PLS-DA (Fig. 18a, b).

3.2.13. *Magmatic apatite grouped by subtypes of igneous rocks*

Apatite from different types of igneous rocks is not well separated by PLS-DA, when compared with carbonatite, metamorphic and sedimentary rocks (Fig. 18). Hence, PLS-DA is used for igneous rocks to determine whether the composition and affinity of magma can be reflected by apatite chemistry. Apatite from different types of igneous rocks cannot be well discriminated in t_1-t_2 (Fig. 19a, b). Apatite samples from intermediate alkaline igneous rocks are mainly located in the negative t_1 region due to positive correlation with Sr, Eu, and V (Fig. 19a, b).

3.2.14. *Apatite grouped by metamorphic grades*

Apatite from high-grade and low- and medium-grade metamorphic rocks can be well discriminated in t_1-t_2 with minor overlapping (Fig. 20a, b). Apatite from low- and medium-grade metamorphic rocks is characterized by positive contributions of V and Sr and negative contributions of low La, Ce, Pr, Nd, Gd, Tb, Dy, and U, in contrast to those from high-grade metamorphic rocks (Fig. 20c, d).

4. Discussion

4.1. *Discrimination between barren rock, ore magmatic, and hydrothermal apatite*

Barren rock, ore magmatic, and hydrothermal apatite independent of deposit types cannot be discriminated from each other (Fig. 7b). In terms of average composition, ore apatite (including magmatic and hydrothermal) has higher contents of As, Y, U, W and lower V, Sr, Zr, Pb, and Ba than barren rock apatite (Fig. 3a, 4d, 7b, e). Hydrothermal apatite has lower total REE and LREE, and higher U, Ba, and W contents than ore

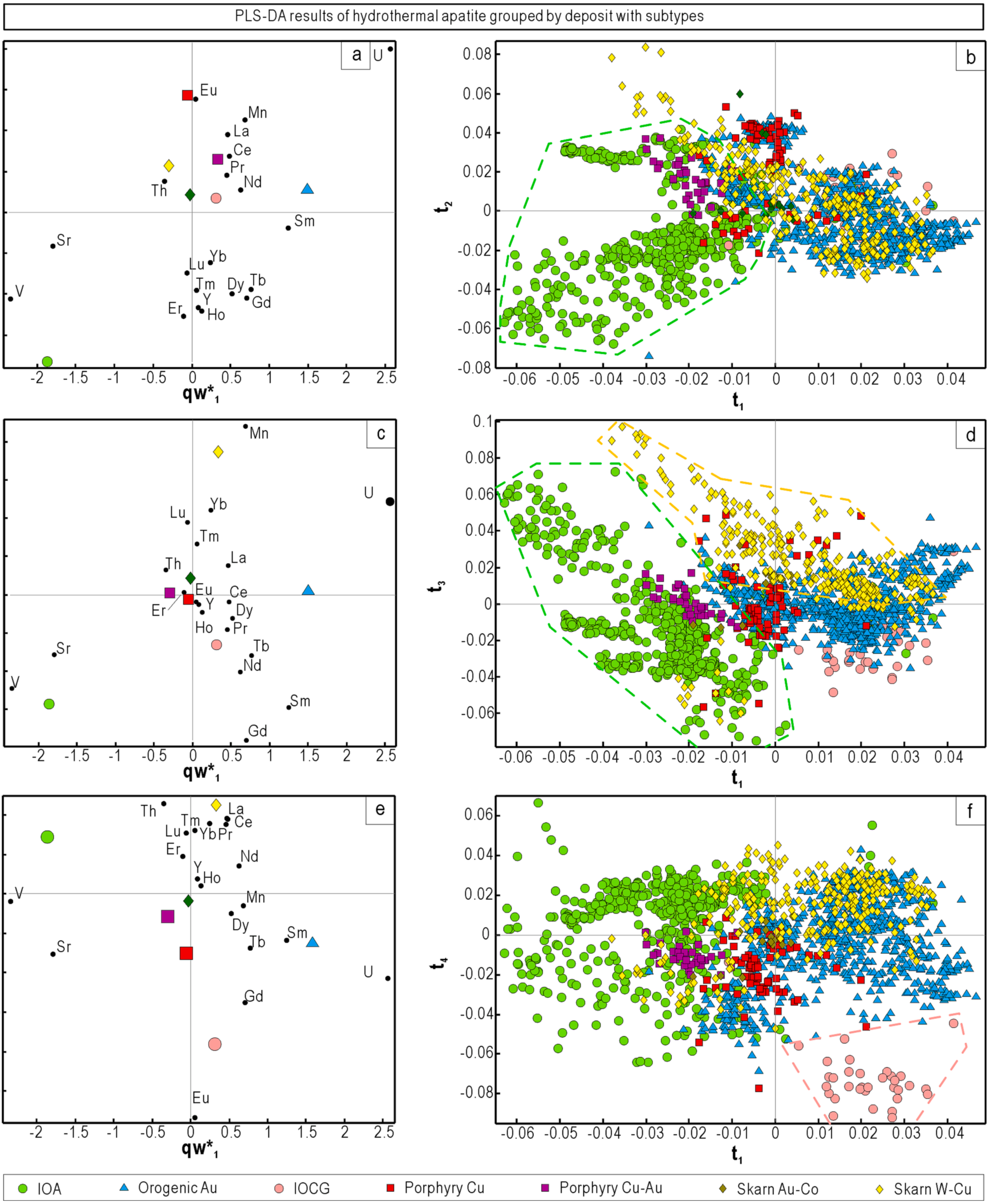

Fig. 14. PLS-DA results of hydrothermal apatite grouped by deposit types with subtypes. Plots of first and second loadings (a), first and third loadings (c), first and fourth loadings (e) showing correlations among elements and deposit types. Plots of first and second scores (b), first and third scores (d), first and fourth scores (f) showing the distribution of individual analyses from different types of deposits in the latent variable space defined in (a), (c) and (e), respectively. (g-i) Score contribution plots of elements for the selected deposit types. (j) The VIP plot showing the importance of elements in classification. For projection of unknown samples, please see the Appendix 3.

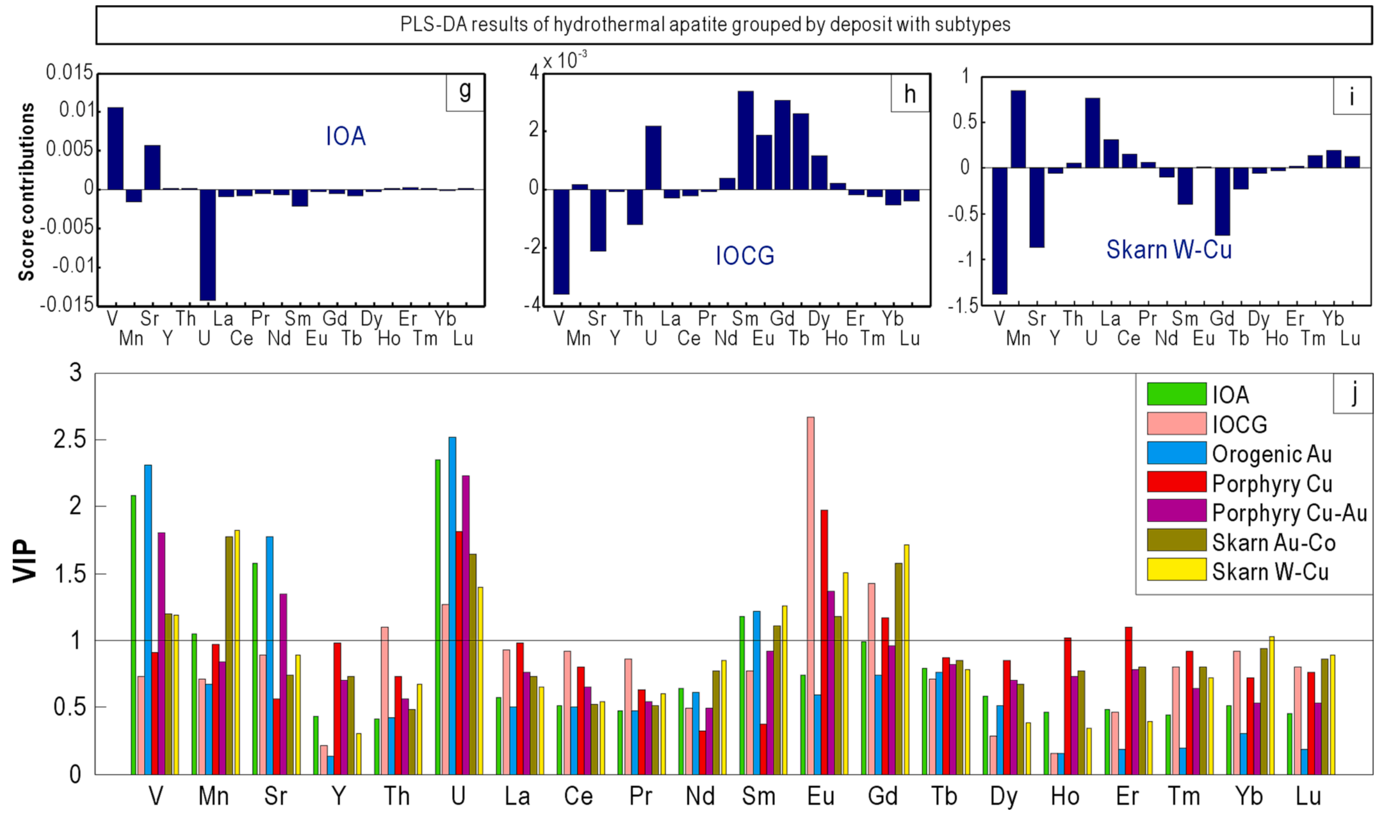

Fig. 14. (*continued*).

magmatic apatite (Fig. 3a, 4d). The compositional overlapping between ore magmatic and hydrothermal apatite from IOCG and IOA deposits (Fig. 8a, b) indicates no obvious chemical boundary between them. Barren magmatic, ore magmatic, and hydrothermal apatite from porphyry deposits are hardly discriminated from each other by PLS-DA (Fig. 10). This is probably due to compositional differences between different subtypes of porphyry deposits (Fig. 16).

Because REE are compatible with apatite crystallized from magma ($D_{REE}^{apatite\text{-}melt} = \sim 1.5$; Klemme and Dalpé, 2003; Prowatke and Klemme, 2006), it is expected that REE will decrease in the residual magma and related hydrothermal solution and form hydrothermal apatite relatively depleted in REE. Moreover, REE will be metasomatically removed from the precursor magmatic or hydrothermal apatite through fluid-mineral action (e.g., dissolution-reprecipitation) to form REE-bearing minerals, such as monazite [(Ce, La, Nd, LREE) PO_4] and xenotime [(Y, HREE) PO_4] (Harlov, 2015; Harlov et al., 2002a; Harlov et al., 2002b; Harlov et al., 2005; Li and Zhou, 2015), resulting in decreased REE contents in newly formed hydrothermal apatite. These expected trends are consistent with the decreased total REE contents from magmatic to hydrothermal apatite. The transition from magmatic apatite to hydrothermal fluorapatite is characterized by an overall increase in HREE concentrations, likely because fluids preferentially combine with LREE at elevated temperatures, resulting in decoupling of LREE and HREE (Mercer et al., 2020; Su et al., 2021). Experience and field works demonstrate that Sr and Mn are fluid mobile elements (Reed et al., 2000; Simon et al., 2007; Williams-Jones and Heinrich, 2005), and are enriched in hydrothermal apatite (La Cruz et al., 2019). The relative enrichment of U and depletion of Th in hydrothermal apatite is consistent with that hydrothermal apatite commonly has higher U/Th ratios than magmatic apatite in IOA deposits (Krneta et al., 2017a; Zeng et al., 2016). Therefore, the PLS-DA result is consistent with the natural and experimental observation of compositional variations between magmatic and hydrothermal apatite.

Barren magmatic and ore magmatic apatite from granitoid-related deposits are well separated by PLS-DA (Fig. 9a, b), due to relatively high V, Sr, Eu, Th, and U for the former and relatively high Mn, La, Ce, Pr, and Nd contents for the latter (Fig. 9). The relative enrichment of Sr and depletion of Mn in barren magmatic apatite likely reflect lower degree of differentiation and more aluminous magma (Chu et al., 2009).

4.2. *Discrimination of magmatic and hydrothermal apatite from different types of deposits*

REE patterns of magmatic apatite commonly exhibit negative or no Eu anomalies (Fig. 6), which are related to the magma oxygen fugacity and feldspar fractionation (Bea and Montero, 1999). However, positive Eu anomalies of magmatic apatite cannot be due to crystal fractionation and likely inherited from magma source (Chu et al., 2009).

Magmatic apatite from granitoid-related, IOA, and granitoid-related deposits can be discriminated but those of skarn, IOCG, and orogenic Au deposits plot in the center of t_1-t_2 and t_1-t_3 (Fig. 11 a-d). Magmatic apatite from IOA deposits is discriminated by relatively high Nd, Sm, Gd, Tb, Dy, and low Mn and U contents (Fig. 11f). Low Mn in apatite from IOA deposits is probably due to crystallization of Mn-compatible magnetite microlites, resulting in the relative depletion of Mn in associated apatite (Knipping et al., 2015). Monazite is the main mineral of IOA deposits rich in LREE, and the crystallization of monazite decreases with increasing ASI (Adlakha et al., 2018; Montel, 1993). Therefore, high HREE contents in IOA magmatic apatite are probably related to peraluminous magmas. Stronger negative Eu anomaly of apatite from IOA deposits (Fig. 6a) is consistent with the lower oxidation state of IOA ore system (Mercer et al., 2020). Magmatic apatite from porphyry deposits is discriminated by relatively high V, Sr, and Eu contents (Fig. 11a, b, g). Relatively high Sr in apatite from porphyry deposits is possibly due to the adakite-like chemical feature of studied porphyry characterized by high Sr contents.

The relatively low Mn contents in magmatic apatite from granitoid-related Cu-Pb-Zn deposits (Fig. 15g) are related to relatively high oxygen fugacity of the host magma (Ding et al., 2015; Miles et al., 2014;

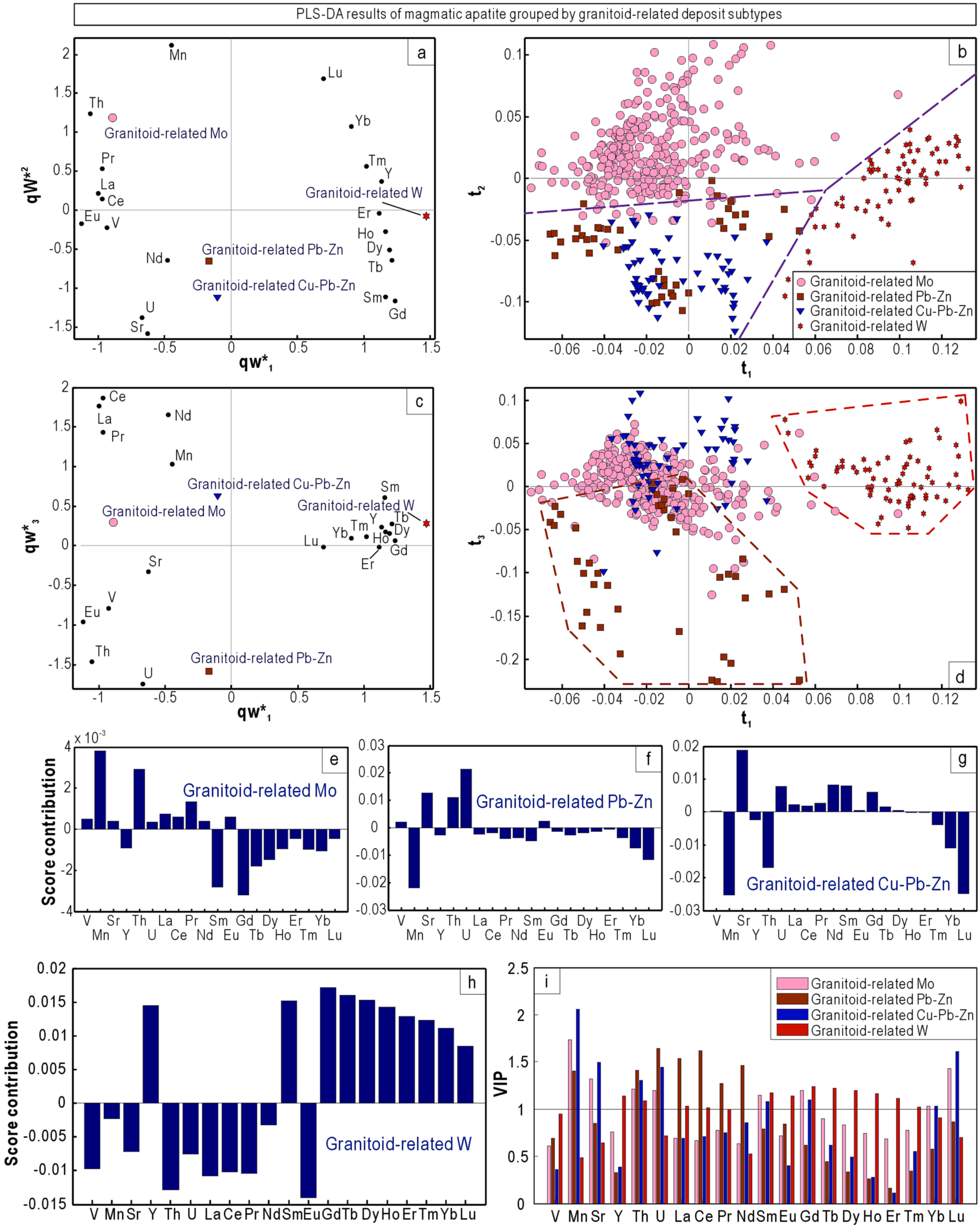

Fig. 15. PLS-DA results of magmatic apatite grouped by subtypes of granitoid-related deposits. Plots of first and second loadings (a), first and third loadings (c) showing correlations among elements and deposit types. Plots of first and second scores (b), first and third scores (d) showing the distribution of individual analyses from different types of deposits in the latent variable space defined in (a) and (c), respectively. (e-h) Score contribution plots of elements for the selected deposit types. (i) The VIP plot showing the importance of elements in classification. For projection of unknown samples, please see the Appendix 3.

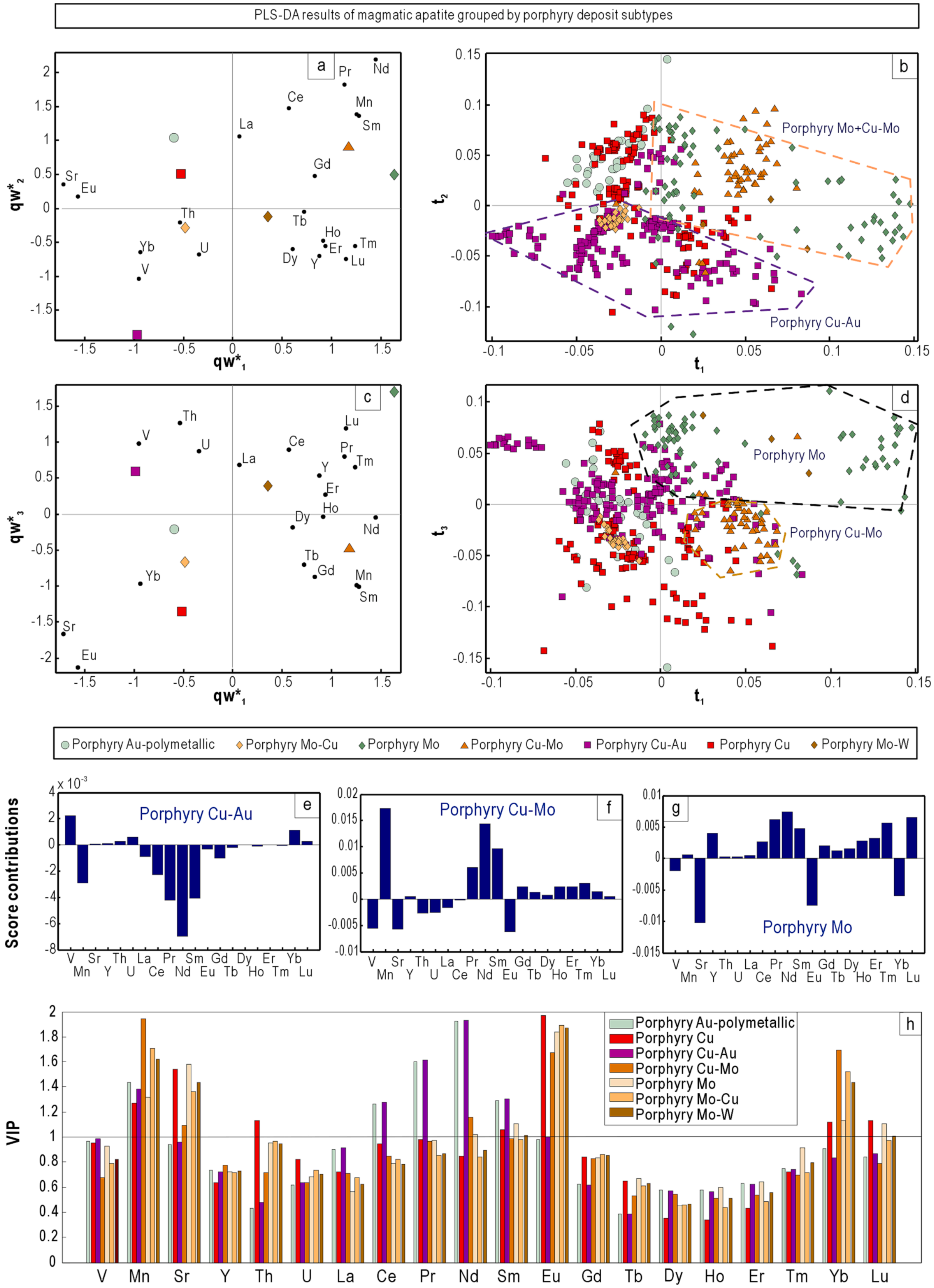

Fig. 16. PLS-DA results of magmatic apatite grouped by subtypes of porphyry deposits. Plots of first and second loadings (a), first and third loadings (c) showing correlations among elements and deposit types. Plots of first and second scores (b), first and third scores (d) showing the distribution of individual analyses from different types of deposits in the latent variable space defined in (a) and (c), respectively. (e-g) Score contribution plots of elements for the selected deposit types. (h) The VIP plot showing the importance of elements in classification. For projection of unknown samples, please see the Appendix 3.

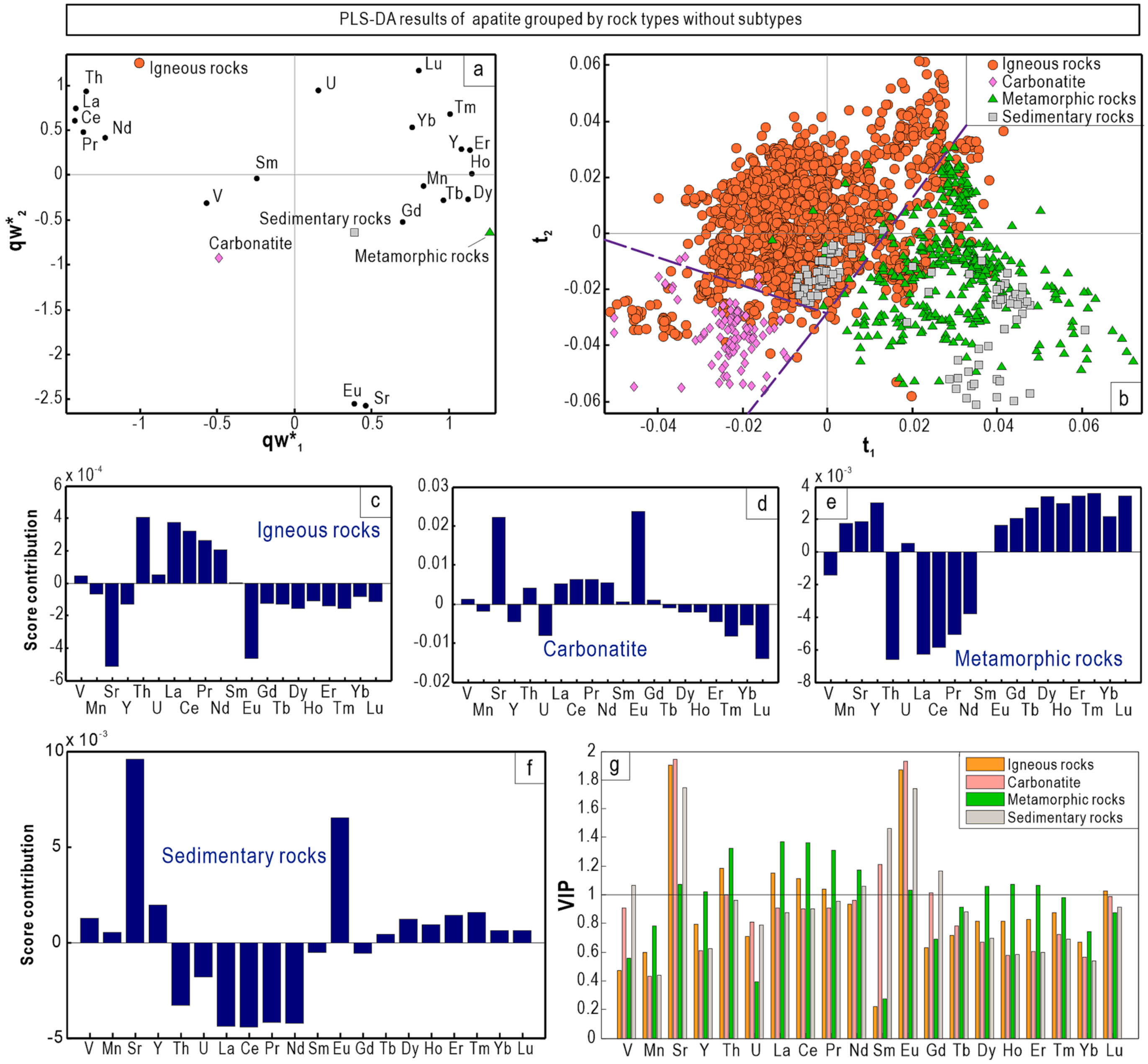

Fig. 17. PLS-DA results of apatite grouped by rock types without subtypes. Plots of first and second loadings (a) showing correlations among elements and deposit types. Plots of first and second scores (b) showing the distribution of individual analyses from different types of rocks in the latent variable space defined in (a). (c-f) Score contribution plots of elements for the selected rock types. (g) The VIP plot showing the importance of elements in classification. For projection of unknown samples, please see the Appendix 3.

Yang et al., 2018). Meanwhile, apatite from granitoid-related Cu-Pb-Zn deposit is distinguished by higher concentration of Sr in comparison to granitoid-related Mo deposit possibly reflecting more mafic magma sources for the former (Belousova et al., 2002; Zafar et al., 2020). Magmatic apatite from Mo-bearing granites is rich in Th (Fig. 15e), likely because the melting of sediments increases the Th content in the magma source (Adlakha et al., 2018; Ding et al., 2015).

The relatively high V and low Mn and Nd contents characterize magmatic apatite from porphyry Cu-Au deposits (Fig. 16e). The Nd depletion is consistent with that subduction-related host rocks have negative anomalies for high field strength elements like Nd (Cao et al., 2022). The relatively low oxygen fugacity of the magma possibly explains the relatively high Mn and low Eu in magmatic apatite from porphyry Cu-Mo and Mo deposits (Cao et al., 2012). The more evolved magma for Mo-mineralization of porphyry deposits accounts for the relatively high contents of Pr, Nd, and Sm and low Sr in magmatic apatite from porphyry Cu-Mo and Cu deposits (Cao et al., 2012; Chen and Zhang, 2018).

Hydrothermal apatite from IOCG, IOA, and skarn deposits can be distinguished from other deposit types (Figs. 12 and 14). Hydrothermal apatite from IOCG deposits has higher U and REE contents than those from IOA deposits (Fig. 3b, 5a, c, and 12), because lower temperature of IOCG deposit cause precipitation of REE in Cl-rich fluid (Williams-Jones and Heinrich, 2005). Relatively low Gd and Tb in hydrothermal apatite from skarn deposits possibly due to the fractionation of Gd and Tb by amphibole, because amphibole preferentially incorporates medium REE over other REE (Adlakha et al., 2018).

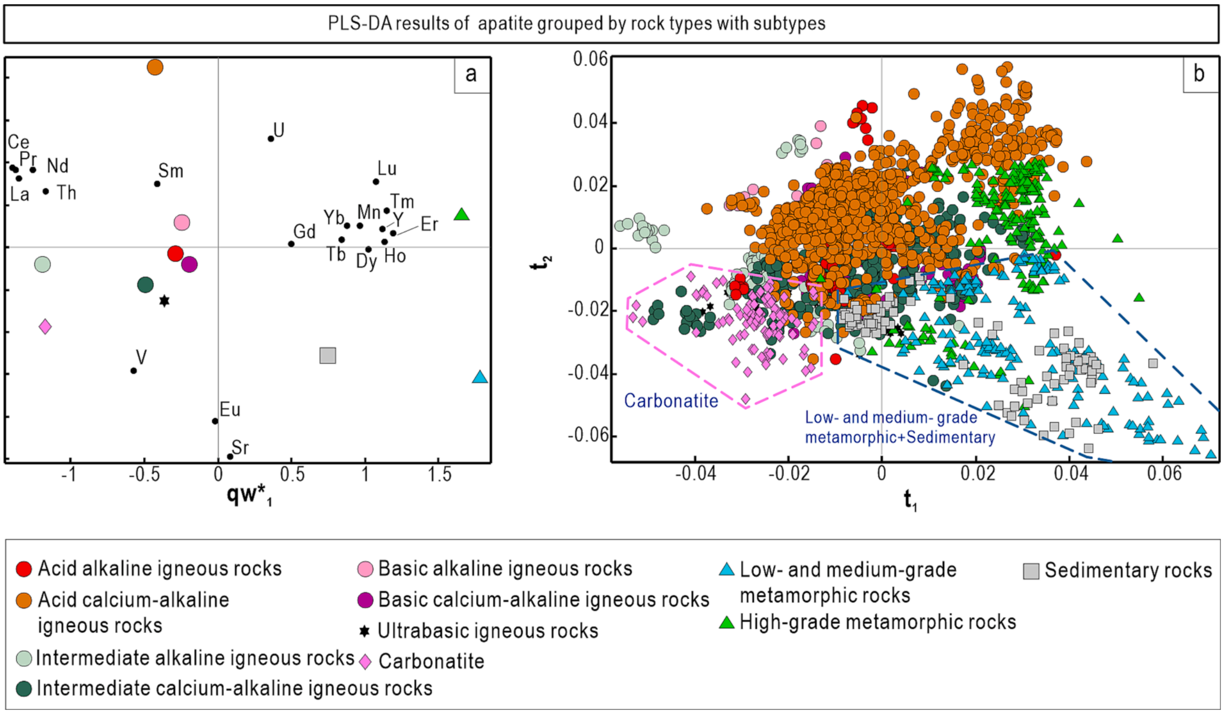

Fig. 18. PLS-DA results of apatite grouped by rock types with subtypes. Plots of first and second loadings (a) showing correlations among elements and deposit types. Plots of first and second scores (b) showing the distribution of individual analyses from different types of rock in the latent variable space defined in (a). For projection of unknown samples, please see Appendix 3.

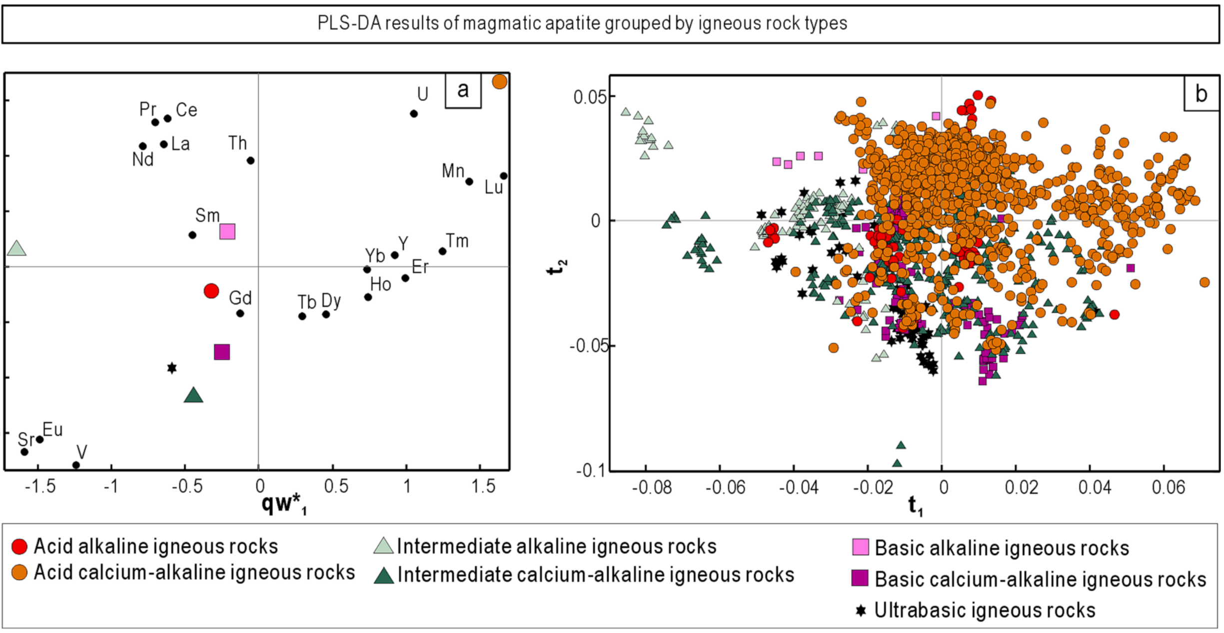

Fig. 19. PLS-DA results of magmatic apatite grouped by igneous rock types. Plots of first and second loadings (a) showing correlations among elements and deposit types. Plots of first and second scores (b) showing the distribution of individual analyses from different types of rock in the latent variable space defined in (a).

4.3. Discrimination apatite from different types of rocks

Experimental studies have demonstrated that partition coefficients of halogens (Doherty et al., 2014; Konzett et al., 2012; Kusebauch et al., 2015; Mathez and Webster, 2005; McCubbin et al., 2015; Webster et al., 2017; Webster et al., 2009) and trace elements (Klemme and Dalpé, 2003; Li and Hermann, 2017; Prowatke and Klemme, 2006; Watson and Green, 1981) between melts and apatite are strongly influenced by melt chemistry. Carbonatitic melts are characterized by high Sr, Ba, and REE abundances (Jones et al., 2013). Most trace elements like REE, Sr, Y, Th, and U show decreased apatite-melt partition coefficients with increasing silica and decreasing Ca and P in melts (Klemme and Dalpé, 2003). Because carbonatitic melts are commonly formed from sediments melting during subduction, the melts are relatively rich in P because sediments contain large amounts of P (Plank and Langmuir 1998). The more Ca-enriched and Si-depleted carbonatitic magma thus explains the

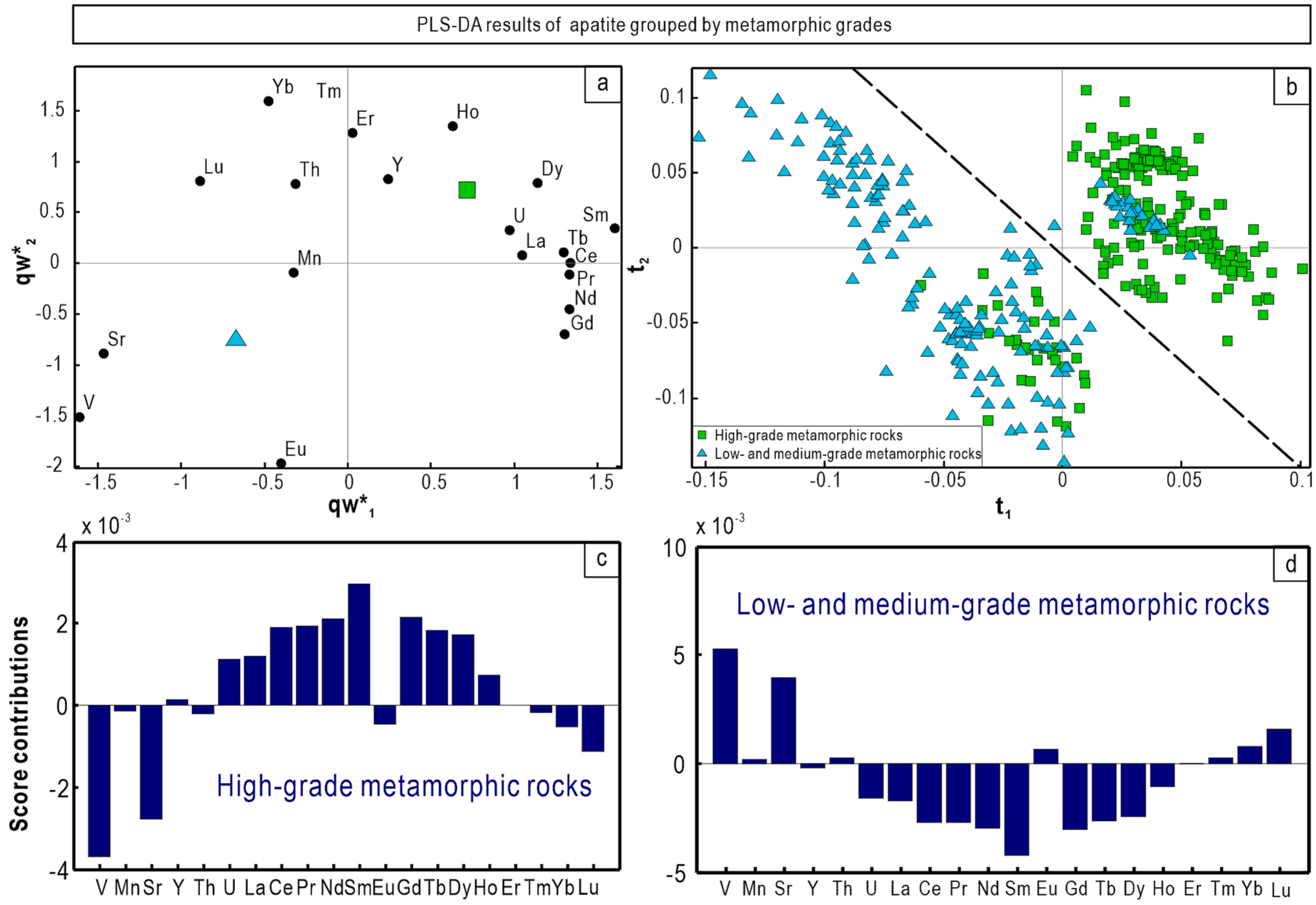

Fig. 20. PLS-DA results of apatite grouped by metamorphic grades. Plots of first and second loadings (a) showing correlations among elements and deposit types. Plots of first and second scores (b) showing the distribution of individual analyses from different metamorphic grades in the latent variable space defined in (a). (c-d) Score contribution plots of elements. For the projection of unknown samples, please see Appendix 3.

higher Sr and REE contents in apatite from carbonatite (Fig. 17d). The REE contents of apatite from sedimentary rocks are lower than igneous rocks and carbonatite (Fig. 5), because surface waters have relatively low concentration of REE (Bea, 1996; Joosu et al., 2016).

Apatite from igneous rocks with different compositions is hard to be discriminated by PLS-DA (Figs. 18 and 19). It is expected there is a regular variation of elements in apatite with ultrabasic to acid based on experimental studies (Klemme and Dalpé, 2003; Prowatke and Klemme, 2006). However, no regular changes in apatite chemistry of ultrabasic to acid and alkaline to calcium alkaline of host rocks were observed. This possibly reflects the different magma sources for these igneous rocks. Apatite from metamorphic rocks can be discriminated by the metamorphic grades (Fig. 20). Higher REE contents in apatite with higher grade of metamorphism are possibly due to the breakdown of hornblende, allanite, and titanite to release REE (Bea and Montero, 1999; Bingen et al., 1996).

4.4. Implication for mineral exploration

Source discrimination is one of the important steps for using indicator minerals in mineral exploration. Previous studies commonly used apatite chemistry to determine the mineralization potential of rocks in a specific region (Cao et al., 2012; Krneta et al., 2017b; Mukherjee et al., 2017; Pan et al., 2016), but whether these rules can be used to other regions remain unknown. Mao et al. (2016) and O'Sullivan et al. (2020) use a larger dataset and considered that discriminant projection analysis (DPA) and principal components analysis (PCA) methods are useful in discriminating apatite from deposit and rock types. This study proposes a new method to discriminate apatite with different origins by multiple steps of PLS-DA (Fig. 21). First, Figs. 11 to 14 are used to discriminate deposit types. Second, Figs. 8-10 are used to discriminate barren magmatic, ore magmatic, and hydrothermal apatite, and Figs. 15 and 16 are used to discriminate subtypes of granitoid-related and porphyry deposits, respectively. In addition to deposit type discrimination, rock type discrimination can be carried out at the same time. Figs. 17 and 18 are used to discriminate rock types. Fig. 20 is further used to distinguish the metamorphic grades of rocks. By combining the above results, the origin of apatite can be determined.

5. Conclusions

Partial least squares-discriminant analysis is used to classify apatite from different origins, magmatic vs hydrothermal, barren vs mineralization, deposit types, and rock types. Barren rock, ore magmatic, and hydrothermal apatite independent of deposit types cannot be separated, however, for specific deposit types (e.g., granitoid-related deposits), these three origins of apatite can be partly separated. Magmatic apatite from granitoid-related, porphyry, and IOA deposits, and IOA deposits can be discriminated from IOCG, skarn, and orogenic Au deposits, whereas hydrothermal apatite from IOCG, IOA and skarn deposits can be distinguished from orogenic and porphyry deposits. Subtypes of granitoid-related, porphyry, and skarn deposits are also further classified. Magmatic apatite from granitoid-related Mo, Pb-Zn, Cu-Pb-Zn, and W deposits is well separated. Magmatic apatite from porphyry Cu-Au,

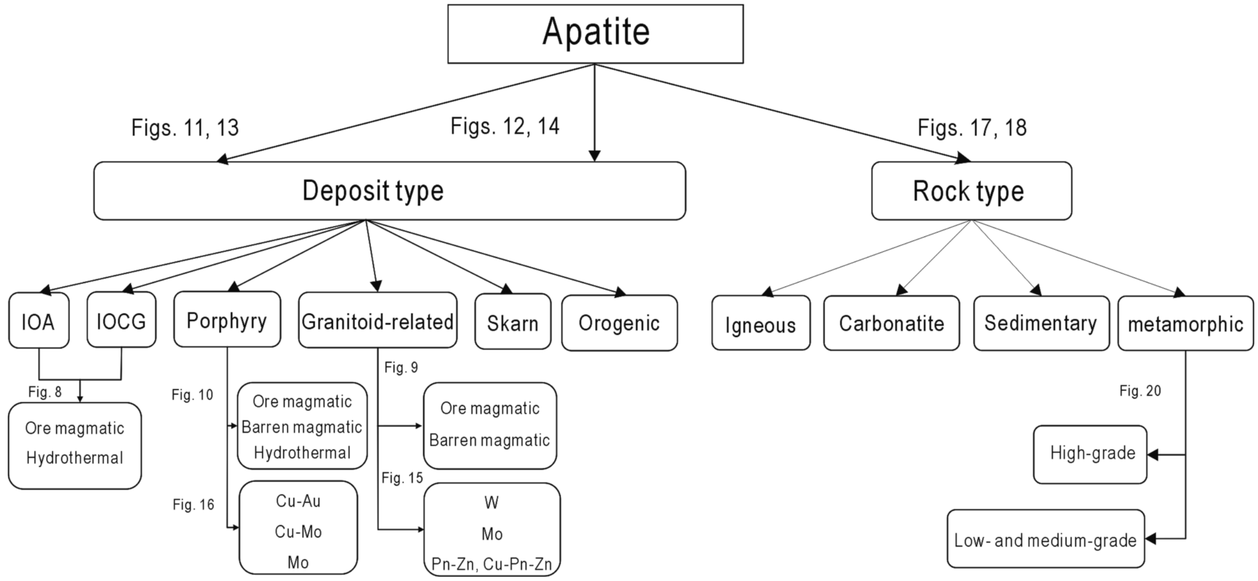

Fig. 21. The flowchart to identify apatite with unknown origins.

Mo, and Cu-Mo deposits are distinguished from other porphyry deposit subtypes. Apatite from igneous rocks, carbonatite, metamorphic rocks, and sedimentary rocks is well discriminated. Different compositions of igneous rocks (from ultrabasic to acidic, alkaline vs calcium-alkaline) cannot be separated. High-grade metamorphic rocks can be discriminated from low- and medium-grade metamorphic rocks. This study demonstrates that apatite chemistry combined with PLS-DA is useful to discriminate apatite with different origins. A flowchart for discriminating apatite with unknown origins is also proposed and can be used in mineral exploration.

Declaration of Competing Interest

The authors declare that they have no known competing financial interests or personal relationships that could have appeared to influence the work reported in this paper.

Data availability

The data that has been used is confidential.

Acknowledgments

This study was supported by funding from CAS Hundred Talents Program to XWH, Field Frontier Key Project of State Key Laboratory of Ore Deposit Geochemistry (202101), and National Natural Science Foundation of China (42173070). We thank two anonymous reviewers who help improve the paper.

Appendix A. Supplementary data

Supplementary data to this article can be found online at https://doi.org/10.1016/j.oregeorev.2022.105269.

References

Adlakha, E., Hanley, J., Falck, H., Boucher, B., 2018. The origin of mineralizing hydrothermal fluids recorded in apatite chemistry at the Cantung W-Cu skarn deposit, NWT, Canada. Eur. J. Mineral. 30, 1095–1113.

Aitchison, J., 1982. The statistical analysis of compositional data. J. Roy. Stat. Soc. Ser. B Methodol. 44, 139–160.

Ayers, J.C., Watson, E.B., 1993. Apatite/fluid partitioning of rare-earth elements and strontium: Experimental results at 1.0 GPa and 1000 °C and application to models of fluid-rock interaction. Chem. Geol. 110, 299–314.

Bea, F., 1996. Residence of REE, Y, Th and U in granites and crustal protoliths; implications for the chemistry of crustal melts. J. Petrol. 37, 521–552.

Bea, F., Montero, P., 1999. Behavior of accessory phases and redistribution of Zr, REE, Y, Th, and U during metamorphism and partial melting of metapelites in the lower crust: an example from the Kinzigite Formation of Ivrea-Verbano, NW Italy. Geochim. Cosmochim. Acta. 63, 1133–1153.

Belousova, E.A., Griffin, W.L., O'Reilly, S.Y., Fisher, N.I., 2002. Apatite as an indicator mineral for mineral exploration: trace-element compositions and their relationship to host rock type. J. Geochem. Explor. 76, 45–69.

Bingen, B., Demaiffe, D., Hertogen, J., 1996. Redistribution of rare earth elements, thorium, and uranium over accessory minerals in the course of amphibolite to granulite facies metamorphism: The role of apatite and monazite in orthogneisses from southwestern Norway. Geochim. Cosmochim. Acta. 60, 1341–1354.

Bouzari, F., Hart, C.J.R., Bissig, T., Barker, S., 2016. Hydrothermal alteration revealed by apatite luminescence and chemistry: A potential indicator mineral for exploring covered porphyry copper deposits. Econ. Geol. 111, 1397–1410.

Brereton, R.G., Lloyd, G.R., 2014. Partial least squares discriminant analysis: taking the magic away. J. Chemometr. 28, 213–225.

Cao, M.J., Li, G.M., Qin, K.Z., Seitmuratova, E.Y., Liu, Y.S., 2012. Major and trace element characteristics of apatites in granitoids from central Kazakhstan: implications for petrogenesis and mineralization. Resour. Geol. 62, 63–83.

Cao, K., Yang, Z.M., White, N.C., Hou, Z.Q., 2022. Generation of the giant porphyry Cu-Au deposit by repeated recharge of mafic magmas at Pulang in Eastern Tibet. Econ. Geol. 117, 57–90.

Chappell, B.W., White, A.J.R., 1992. I- and S-type granites in the Lachlan Fold Belt. Earth Environ Sci. Trans. Roy. Soc. Edinburgh. 83, 1–26.

Chen, L., Zhang, Y., 2018. In situ major-, trace-elements and Sr-Nd isotopic compositions of apatite from the Luming porphyry Mo deposit, NE China: constraints on the petrogenetic-metallogenic features. Ore Geol. Rev. 94, 93–103.

Chu, M.F., Wang, K.L., Griffin, W.L., Chung, S.L., O'Reilly, S.Y., Pearson, N.J., Iizuka, Y., 2009. Apatite composition: tracing petrogenetic processes in transhimalayan granitoids. J. Petrol. 50, 1829–1855.

De Iorio, M., Ebbels, T.M.D., Stephens, D.A., 2007. Statistical techniques in metabolic profiling. In: Balding, D.J., Bishop, M., Cannings, C. (Eds.), Handbook of Statistical Genetics, (Third Edition). John Wiley & Sons Ltd, pp. 347–373.

Ding, T., Ma, D., Lu, J., Zhang, R., 2015. Apatite in granitoids related to polymetallic mineral deposits in southeastern Hunan Province, Shi-Hang zone, China: implications for petrogenesis and metallogenesis. Ore Geol. Rev. 69, 104–117.

Doherty, A.L., Webster, J.D., Goldoff, B.A., Piccoli, P.M., 2014. Partitioning behavior of chlorine and fluorine in felsic melt–fluid(s)–apatite systems at 50MPa and 850–950 °C. Chem. Geol. 384, 94–111.

Egozcue, J.J., Pawlowsky-Glahn, V., Mateu-Figueras, G., Barceló-Vidal, C., 2003. Isometric logratio transformations for compositional data analysis. Math. Geol. 35, 279–300.

Elliott, J.C., 2002. Calcium phosphate biominerals. Rev. Mineral. Geochem. 48, 427–453.

Eriksson, L., Byrne, T., Johansson, E., Trygg, J., Vikström, C., 2013. Multi-and megavariate data analysis basic principles and applications. MKS Umetrics AB, Sweden.

Harlov, D.E., 2015. Apatite: A fingerprint for metasomatic processes. Elements 11, 171–176.

Harlov, D.E., Andersson, U.B., Förster, H.J., Nyström, J.O., Dulski, P., Broman, C., 2002. Apatite–monazite relations in the Kiirunavaara magnetite–apatite ore, northern Sweden. Chem. Geol. 191, 47–72.

Harlov, D.E., Wirth, R., Förster, H.-J., 2005. An experimental study of dissolution–reprecipitation in fluorapatite: fluid infiltration and the formation of monazite. Contrib. Mineral. Petrol. 150, 268–286.

Harlov, D.E., Förster, H.-J.R., Nijland, T.G., 2002. Fluid-induced nucleation of (Y + REE)-phosphate minerals within apatite: Nature and experiment. Part I. Chlorapatite. Am. Mineral. 87, 245–261.

Helsel, D.R., 2005. Nondetects and data analysis: Statistics for censored environmental data. Wiley-Interscience, New York.

Hron, K., Templ, M., Filzmoser, P., 2010. Imputation of missing values for compositional data using classical and robust methods. Computat. Stat. Data Anal. 54, 3095–3107.

Huang, X.W., Boutroy, É., Makvandi, S., Beaudoin, G., Corriveau, L., De Toni, A.F., 2019. Trace element composition of iron oxides from IOCG and IOA deposits: relationship to hydrothermal alteration and deposit subtypes. Miner. Deposita 54, 525–552.

Hughes, J.M., Rakovan, J., 2002. The crystal structure of apatite, $Ca_5(PO_4)_3(F, OH, Cl)$. Rev. Mineral. Geochem. 48, 1–12.

Jiang, X.Y., Li, H., Ding, X., Wu, K., Guo, J., Liu, J.Q., Sun, W.D., 2018. Formation of A-type granites in the Lower Yangtze River Belt: A perspective from apatite geochemistry. Lithos. 304–307, 125–134.

Jones, A.P., Genge, M., Carmody, L., 2013. Carbonate melts and carbonatites. Rev. Mineral. Geochem. 75, 289–322.

Joosu, L., Lepland, A., Kreitsmann, T., Üpraus, K., Roberts, N.M.W., Paiste, P., Martin, A. P., Kirsimäe, K., 2016. Petrography and the REE-composition of apatite in the Paleoproterozoic Pilgujärvi Sedimentary Formation, Pechenga Greenstone Belt, Russia. Geochim. Cosmochim. Acta 186, 135–153.

Klemme, S., Dalpé, C., 2003. Trace-element partitioning between apatite and carbonatite melt. Am. Mineral. 88, 639–646.

Knipping, J.L., Bilenker, L.D., Simon, A.C., Reich, M., Barra, F., Deditius, A.P., Wälle, M., Heinrich, C.A., Holtz, F., Munizaga, R., 2015. Trace elements in magnetite from massive iron oxide-apatite deposits indicate a combined formation by igneous and magmatic-hydrothermal processes. Geochim. Cosmochim. Acta 171, 15–38.

Konzett, J., Rhede, D., Frost, D.J., 2012. The high PT stability of apatite and Cl partitioning between apatite and hydrous potassic phases in peridotite: an experimental study to 19 GPa with implications for the transport of P, Cl and K in the upper mantle. Contrib. Mineral. Petrol. 163, 277–296.

Krneta, S., Ciobanu, C.L., Cook, N.J., Ehrig, K., Kontonikas-Charos, A., 2017a. Rare earth element behaviour in apatite from the Olympic dam Cu–U–Au–Ag deposit, South Australia. Minerals 7, 135.

Krneta, S., Cook, N.J., Ciobanu, C.L., Ehrig, K., Kontonikas-Charos, A., 2017b. The Wirrda Well and Acropolis prospects, Gawler Craton, South Australia: insights into evolving fluid conditions through apatite chemistry. J. Geochem. Explor. 181, 276–291.

Kusebauch, C., John, T., Whitehouse, M.J., Klemme, S., Putnis, A., 2015. Distribution of halogens between fluid and apatite during fluid-mediated replacement processes. Geochim. Cosmochim. Acta. 170, 225–246.

La Cruz, N.L., Simon, A.C., Wolf, A.S., Reich, M., Barra, F., Gagnon, J.E., 2019. The geochemistry of apatite from the Los Colorados iron oxide–apatite deposit, Chile: implications for ore genesis. Miner. Deposita. 54, 1143–1156.

Li, H., Hermann, J., 2017. The effect of fluorine and chlorine on trace element partitioning between apatite and sediment melt at subduction zone conditions. Chem. Geol. 473, 55–73.

Li, X., Zhou, M.-F., 2015. Multiple stages of hydrothermal REE remobilization recorded in fluorapatite in the Paleoproterozoic Yinachang Fe–Cu–(REE) deposit, Southwest China. Geochim. Cosmochim. Acta 166, 53–73.

Makvandi, S., Ghasemzadeh-Barvarz, M., Beaudoin, G., Grunsky, E.C., McClenaghan, M. B., Duchesne, C., Boutroy, E., 2016. Partial least squares-discriminant analysis of trace element compositions of magnetite from various VMS deposit subtypes: Application to mineral exploration. Ore Geol. Rev. 78, 388–408.

Mao, M., Rukhlov, A.S., Rowins, S.M., Spence, J., Coogan, L.A., 2016. Apatite trace element compositions: A robust new tool for mineral exploration. Econ. Geol. 111, 1187–1222.

Mathez, E.A., Webster, J.D., 2005. Partitioning behavior of chlorine and fluorine in the system apatite-silicate melt-fluid. Geochim. Cosmochim. Acta 69, 1275–1286.

McCubbin, F.M., Vander Kaaden, K.E., Tartèse, R., Boyce, J.W., Mikhail, S., Whitson, E. S., Bell, A.S., Anand, M., Franchi, I.A., Wang, J., Hauri, E.H., 2015. Experimental investigation of F, Cl, and OH partitioning between apatite and Fe-rich basaltic melt at 1.0–1.2 GPa and 950–1000°C. Am. Mineral. 100, 1790–1802.

Mercer, C.N., Watts, K.E., Gross, J., 2020. Apatite trace element geochemistry and cathodoluminescent textures—A comparison between regional magmatism and the Pea Ridge IOAREE and Boss IOCG deposits, southeastern Missouri iron metallogenic province, USA. Ore Geol. Rev. 116, 103129.

Miles, A.J., Graham, C.M., Hawkesworth, C.J., Gillespie, M.R., Hinton, R.W., Bromiley, G.D., EMMAC, 2014. Apatite: A new redox proxy for silicic magmas? Geochim. Cosmochim. Acta 132, 101–119.

Montel, J.M., 1993. A model for monazite/melt equilibrium and application to the generation of granitic magmas. Chem. Geol. 110, 127–146.

Mukherjee, R., Venkatesh, A.S., Fareeduddin, 2017. Chemistry of magnetite-apatite from albitite and carbonate-hosted Bhukia Gold Deposit, Rajasthan, western India – An IOCG-IOA analogue from Paleoproterozoic Aravalli Supergroup: evidence from petrographic, LA-ICP-MS and EPMA studies. Ore Geol. Rev. 91, 509–529.

O`Sullivan, G., Chew, D., Kenny, G., Henrichs, I., Mulligan, D., 2020. The trace element composition of apatite and its application to detrital provenance studies. Earth Sci. Rev. 201, 103044.

Pan, L.C., Hu, R.Z., Wang, X.S., Bi, X.W., Zhu, J.J., Li, C., 2016. Apatite trace element and halogen compositions as petrogenetic-metallogenic indicators: Examples from four granite plutons in the Sanjiang region, SW China. Lithos. 254–255, 118–130.

Piccoli, P.M., Candela, P.A., 2002. Apatite in igneous systems. Rev. Mineral. Geochem. 48, 255–292.

Plank, T., Langmuir, C.H., 1998. The chemical composition of subducting sediment and its consequences for the crust and mantle. Chem. Geol. 145, 325–394.

Prowatke, S., Klemme, S., 2006. Trace element partitioning between apatite and silicate melts. Geochim. Cosmochim. Acta 70, 4513–4527.

Reed, M.J., Candela, P.A., Piccoli, P.M., 2000. The distribution of rare earth elements between monzogranitic melt and the aqueous volatile phase in experimental investigations at 800 °C and 200 MPa. Contrib. Mineral. Petrol. 140, 251–262.

Sha, L.K., Chappell, B.W., 1999. Apatite chemical composition, determined by electron microprobe and laser-ablation inductively coupled plasma mass spectrometry, as a probe into granite petrogenesis. Geochim. Cosmochim. Acta 63, 3861–3881.

Simon, A.C., Pettke, T., Candela, P.A., Piccoli, P.M., Heinrich, C.A., 2007. The partitioning behavior of As and Au in S-free and S-bearing magmatic assemblages. Geochim. Cosmochim. Acta 71, 1764–1782.

Su, Z.K., Zhao, X.F., Li, X.C., Zhou, M.F., Kennedy, A.K., Zi, J.W., Spandler, C., Yang, Y. H., 2021. Unraveling mineralization and multistage hydrothermal overprinting histories by integrated in situ U-Pb and Sm-Nd isotopes in a paleoproterozoic breccia-hosted iron oxide copper-gold deposit, SW China. Econ. Geol. 116, 1687–1710.

Watson, E.B., Green, T.H., 1981. Apatite/liquid partition coefficients for the rare earth elements and strontium. Earth Planet. Sci. Lett. 56, 405–421.

Webster, J.D., Piccoli, P.M., 2015. Magmatic apatite: A powerful, yet deceptive. Mineral. Elements 11, 177–182.

Webster, J.D., Tappen, C.M., Mandeville, C.W., 2009. Partitioning behavior of chlorine and fluorine in the system apatite–melt–fluid. II: Felsic silicate systems at 200MPa. Geochim. Cosmochim. Acta 73, 559–581.

Webster, J.D., Goldoff, B.A., Flesch, R.N., Nadeau, P.A., Silbert, Z.W., 2017. Hydroxyl, Cl, and F partitioning between high-silica rhyolitic melts-apatite-fluid(s) at 50–200 MPa and 700–1000 °C. Am. Mineral. 102, 61–74.

Whitten, E.H.T., 1995. Open and closed compositional data in petrology. Math Geol. 27, 789–806.

Williams-Jones, A.E., Heinrich, C.A., 2005. Vapor transport of metals and the formation of magmatic-hydrothermal ore deposits: 100th Anniversary Special Paper. Econ. Geol. 100, 1287–1312.

Wold, S., Sjöström, M., Eriksson, L., 2001. PLS-regression: a basic tool of chemometrics. Chemom. Intell. Lab. Syst. 58, 109–130.

Xing, K., Shu, Q., Lentz, D.R., 2021. Constraints on the formation of the Giant Daheishan Porphyry Mo Deposit (NE China) from whole-rock and accessory mineral geochemistry. J. Petrol. 62, 1–26.

Yang, J.H., Kang, L.F., Peng, J.T., Zhong, H., Gao, J.F., Liu, L., 2018. In-situ elemental and isotopic compositions of apatite and zircon from the Shuikoushan and Xihuashan granitic plutons: Implication for Jurassic granitoid-related Cu-Pb-Zn and W mineralization in the Nanling Range, South China. Ore Geol. Rev. 93, 382–403.

Zafar, T., Rehman, H.U., Mahar, M.A., Alam, M., Oyebamiji, A., Rehman, S.U., Leng, C.-B., 2020. A critical review on petrogenetic, metallogenic and geodynamic implications of granitic rocks exposed in north and east China: New insights from apatite geochemistry. J. Geodyn. 136, 101723.

Zeng, L.P., Zhao, X.F., Li, X.C., Hu, H., McFarlane, C., 2016. In situ elemental and isotopic analysis of fluorapatite from the Taocun magnetite-apatite deposit, Eastern China: Constraints on fluid metasomatism. Am. Mineral. 101, 2468–2483.